Characteristics and Stability of
SOI-Based Silicon Nanowire FET Sensors

Björn Niesen

August 5, 2008

UNI
BASEL

Contents

Chapter 1

Introduction

1.1 Motivation

About 35 years ago, the concept of the ion-sensitive field effect transistor (ISFET) was introduced [1]. An ISFET uses the field effect to detect changes in the electrostatic potential caused by ions in the vicinity of the sensor surface [2]. By coating the sensor surface with enzymes [3, 4] or single stranded DNA [5, 6], this sensor is capable of detecting the binding of specific target molecules. In contrast to the widely used fluorescence-based detection of biomolecules [7], ISFET sensors do not require time-consuming and expensive labeling of the targets.

Recently, the ISFET concept has been transferred to FET nanosensors [8], that allow the integration of dense arrays of sensors [9, 10, 11]. Therefore systems based on FET nanosensors promise low-cost, high-throughput analysis of biological reactions. Furthermore, FET nanosensors are particularly attractive as biosensors as their critical dimensions are comparable to the size of biological and chemical species. Due to the large surface-to-volume ratio, electrical properties such as the conductance of such FET nanosensors are dominated by surface influences. This greatly enhances the detection sensitivity [12].

A variety of FET nanosensors has been proposed, including silicon nanowires (SiNWs) [13, 14], silicon nanoribbons [15], semiconducting carbon nanotubes [16, 17] and nanogaps [18, 19]. Generally, two different approaches exist: these nanoscale structures can either be assembled from atoms or molecules (bottom-up approach) or fabricated by etching a macro-scaled material (top-down approach). The bottom-up approach allows the fabrications of much smaller structures but is not compatible to complementary metal oxide semiconductor (CMOS) processes. Carbon nanotubes and grown silicon nanowires both suffer from this drawback. Therefore, CMOS compatible top-down SiNW fabrication protocols have been developed [20, 21, 22]. Such SiNWs are usually based on silicon-on-insulator (SOI) wafers, that offer silicon and SiO_2 layers with thickness of a few nanometers [23].

Although SiNW have been the subject of intense research within the past few years and promising results have been obtained with SiNW sensors, many aspects concerning the sensing mechanism of SiNW FETs still require further investigation. Such basic

aspects include the influence of the ion concentration [24, 25] or the pH value of a solution [26], as well as the effects of the geometry [27, 28] and the doping density [29] of SiNWs.

1.2   About this project

This project continued the work done by Dino Keller [20] and Oren Knopfmacher [30], who developed a scalable SOI-based CMOS-compatible SiNW fabrication protocol and characterized the nanowires fabricated by this protocol. The work also included measurements in electrolytes. Thereby a measurement set-up was used that allowed to influence the SiNW conductance by a back-gate and an electrolyte-gate simultaneously. This dual-gating approach was found to provide a well-controlled environment for sensing experiments.

This set-up was gradually modified during this project to improve the electrolyte-gate stability and to allow the measurements of SiNWs in parallel. Initial measurements were conducted using the unmodified set-up and SiNWs, that had been fabricated during the previous work, in order to continue their characterization. Further measurements with these SiNWs were performed to examine the improvements due to the set-up modifications.

At the same time, new SiNWs were fabricated using the above mentioned protocol with some modifications. These nanowires were finally characterized in air as well as in solution. Furthermore, their sensing capability was examined by measuring the influence of the ion concentration and the pH value of the solution.

Chapter 2

Silicon nanowire fabrication

In order to fabricate SiNW sensors a CMOS compatible protocol had been developed, successfully applied and described in detail by Dino Keller [20] and Oren Knopfmacher [30]. However, several unsuccessful attempts to reproduce functional nanowires following this initial protocol unveiled a number of steps that had to be altered to reach a better reproducibility. This modified fabrication protocol will be presented in the following. A detailed list of all fabrication steps and parameters as well as a discussion of the modifications made can be found in the appendix.

2.1 Modified fabrication protocol

SiNWs were fabricated by selectively etching different layers of a SOI wafer. Such a wafer consists of several alternating silicon and silicon oxide layers, as shown in Figure 2.1 a. The (100) oriented silicon layers are p-doped by boron with a resistivity of 10-20 Ωcm, which corresponds to a doping density of about 10^{15} cm^{-3}. The topmost layer, the 68 nm thick top oxide had been formed by thermal oxidation (Figure 2.1 b). During the fabrication process, this layer acts as an etch mask. A silicon layer with a thickness of about 70 nm lies beneath it. This so-called device layer will form the silicon nanowires. This device layer is separated by the silicon substrate by a buried oxide (BOX) layer, which is about 152 nm thick. The BOX was obtained by oxygen implantation (SIMOX process [23]). This insulating layer is necessary as the silicon substrate will be used as a back-gate to modulate the charge carrier density in the SiNW. The thickness of the individual layers was examined by ellipsometry (SiO$_2$ thickness was fitted by using the Palik model, Si by the Jellison model) and was found to be homogeneous throughout the wafer with a variation of about $\pm$0.5 nm.

A sufficiently large piece was cut out of such a SOI wafer. This piece was then cleaned by sonication in acetone and isopropanol, followed by a UV/ozone treatment and another sonication in acetone and isopropanol. The cleaned sample was then processed as follows:

a) Starting SOI wafer

e) Cr mask removed

b) Thermal oxidation of top oxide

f) Si device layer etched

c) Cr mask

g) Contact region defined

d) Top oxide etched

h) Contact Al deposited
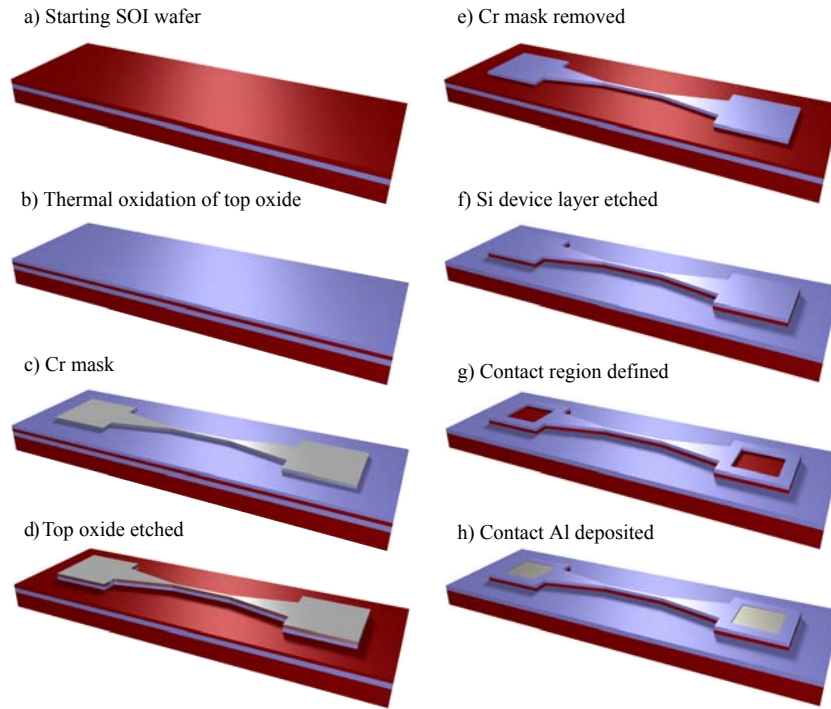
Figure 2.1: Fabrication steps of a SiNW: a) The process starts from a SOI wafer consisting of a silicon device layer (red) on a layer of buried oxide (blue) and the silicon substrate (red) at the bottom. b) A top oxide layer (blue) is applied onto the device layer by thermal oxidation. c) The nanowire and the leads are defined by e-beam lithography and chromium evaporation (gray). d) This pattern is transferred into the top oxide by CHF$_3$ and oxygen plasma. e, f) After the chromium etch mask has been removed the device layer is etched by TMAH. The patterned top oxide thereby acts as etch mask. g, h) In order to contact the nanowire, rectangular shapes are patterned by UV lithography and the top oxide is removed at those areas by HF. Aluminum contact pads (gray) are deposited directly onto the device layer by evaporation. By an annealing step, ohmic contacts are formed between the aluminum and the silicon device layer. Adapted from [20].

2.1.1 E-beam lithography

A layer of poly(methyl methacrylate) (PMMA) with a thickness of about 320 nm was spun on the sample from chlorobenzene and hardened by baking the sample for 30 minutes at 170° C. In order to pattern the PMMA layer, two e-beam lithography steps were performed. During the first step the nanowires were patterned, during the second step a higher probe current and a larger step size was chosen to pattern larger structures such as the leads and alignment crosses. The shapes of these two masks can be seen in Figure 2.2. Six wires were patterned by writing 100, 125...200 and 1000 nm wide rectangles. One nanowire was patterned by writing a line. All nanowire patterns were 10 μm long. The long axis of the SiNWs were aligned along a <110> direction.

After the e-beam exposure, the samples were developed in a solution of methyl isobutyl ketone (MIBK) and isopropanol with ratio 1:3 for 90 s.
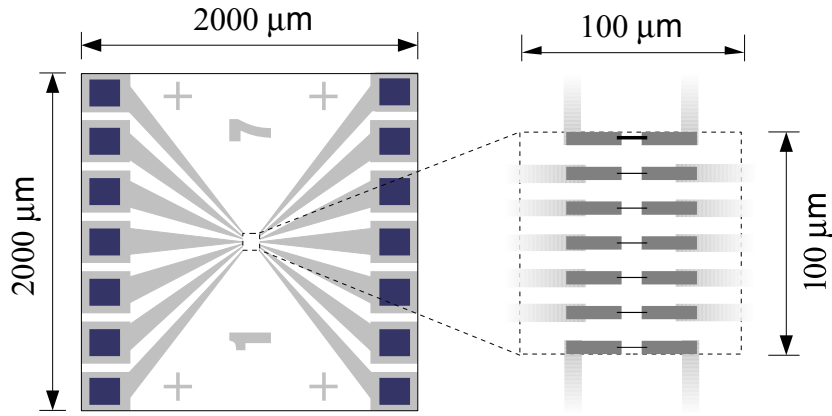
Figure 2.2: Left: Schematic of lithography masks for leads (gray) and contact pads (blue), patterned by e-beam and UV lithography, respectively. This mask has a size of about 2×2 mm Right: E-beam mask for nanowires (black) and rectangular structures (gray) to connect them with the leads patterned by the larger mask. The topmost nanowire pattern has a width of 1μm, the nanowire pattern at the bottom was written as line. The other nanowires had a width of 100, 125..200 nm, respectively.

2.1.2 Chromium evaporation

A 60 nm thick chromium layer was deposited by evaporation at deposition rates between 0.1-0.2 nm/s (Figure 2.1 c). Usually the pressure during evaporation was about $5 \cdot 10^{-7}$ mbar and the temperature was around 0° C. The sample surface was oriented perpendicular to the chromium source. A lift-off in acetone at 45° C removed all chrome except for the areas that had been exposed to the e-beam previously.

2.1.3   Silicon oxide etch

In order to transfer the chromium pattern into the top oxide layer of the sample, a series of plasma etch steps was performed (Figure 2.1 d). An initial oxygen plasma removed any leftover PMMA from the sample surface. CHF_3 plasma was used to etch the top oxide. A small quantity of oxygen was added during the first minutes to obtain a smoother surface. As this combination of CHF_3 and O_2 also etches silicon, the last few nm of the top oxide were etched by pure CHF_3 plasma in order to protect the silicon device layer beneath it [20]. Finally, another oxygen plasma was applied to be sure that all PMMA has been removed. Once the pattern had been transferred into to top oxide, the chromium was removed by a solution of NaOH and $KMnO_4$ in H_2O (Figure 2.1 e). This mixture efficiently etches chromium as well as chromium oxide but does neither attack silicon nor silicon oxide.

2.1.4   Silicon etch

The patterned top oxide then was used as an etch mask while etching the silicon device layer using tetramethyl ammonium hydroxide (TMAH) (Figure 2.1 f). As TMAH etches SiO_2 very slowly [31], the sample was dipped into buffered hydrofluoric acid (HF) for about 20 s in order to remove the native oxide on the device layer. The device layer itself was then etched in an aqueous solution of TMAH and isopropanol at 45° C while vigorous stirring. The addition of isopropanol results in smoother etched surfaces [32]. As TMAH etches (100) surfaces much faster than those that lie in the (111) plane [33], the device layer is completely removed at all areas that had not been covered by the top oxide, whereas the protected areas are only slowly underetched (Figure 2.3). Due to this anisotropic etching, well defined nanowires with (111) oriented side walls are formed. This well defined shape is visible in scanning electron microscope (SEM) images (Figure 2.1.4).

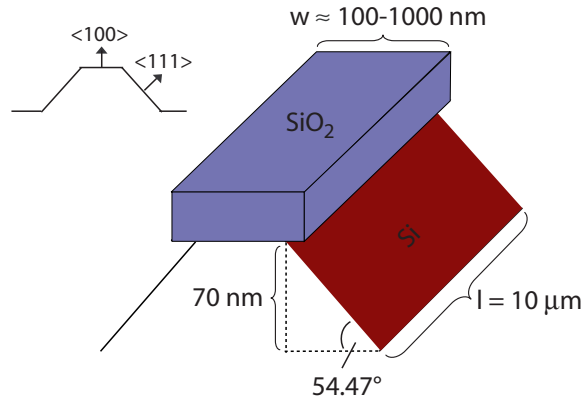Figure 2.3: Geometry of a SiNW. The trapezoid-shaped nanowire cross section is caused by the anisotropic etching of silicon in TMAH. As (111) silicon surfaces are only slowly etched by TMAH, the nanowire side walls lie in (111) planes, with an angle of about 55° relative to the wafer surface, which is (100) oriented. SiO_2 acts as etch mask. The height of the SiNW is given by the silicon device layer thickness of about 70 nm.
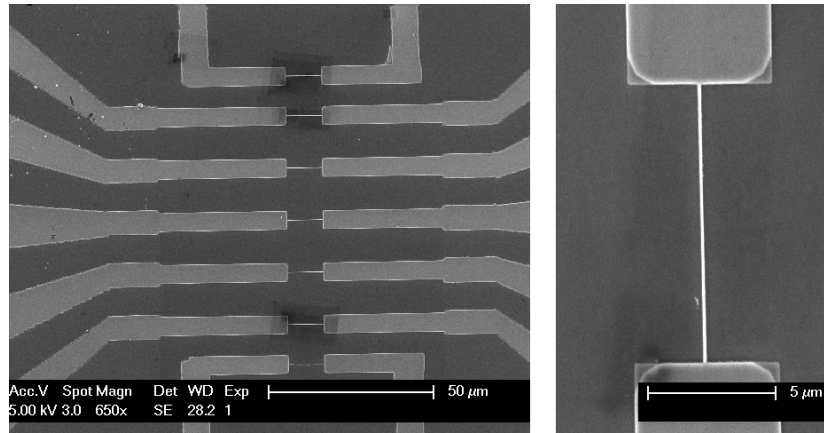
Figure 2.4: SEM micrographs of the center of the sample. Left: The seven nanowires are visible as horizontal lines, the leads to the contacts of the two outermost nanowires enter the image from the top and the bottom, the other nanowires are connected by horizontal leads. The thickness of the SiNW decreases from top to bottom. Right: Image of the second thinnest SiNW.

The final width of nanowires that had been patterned by writing 100 and 125 nm wide rectangles using e-beam lithography, was examined by atomic force microscopy (AFM) (Figure 2.5). A width between 97 and 106 nm and from 129 to 136 nm was measured at the top of the "100 nm" and the "125 nm" nanowire by examining the cross section at different areas of the wires. The width at the bottom was around 260 nm and 360 nm, respectively. The height of both nanowires was around 120 nm.

As the width of the top oxide is close to the expected value, the combination of e-beam lithography, chromium evaporation, lift-off and plasma etching seems to work fine. The slightly larger width could be due to scattering of electrons within the PMMA. The width at the bottom of the nanowires is larger than the expected 200 nm and 225 nm, respectively. This could however be an artifact of the AFM, as the cone-shaped AFM tip has a finite opening angle, which limits the lateral resolution. Probably for the same reason, the transition between the top oxide, which should have nearly vertical side walls, and the semiconducting part of the nanowire with its trapezoidal cross section is not visible. The height of about 120 nm is about 17 nm smaller than the sum of top oxide and device layer of the initial wafer. As the buffered HF etches SiO_2 with about 40 nm/min [20] and the sample was exposed about 20 s, the measure height is close of the expected value.
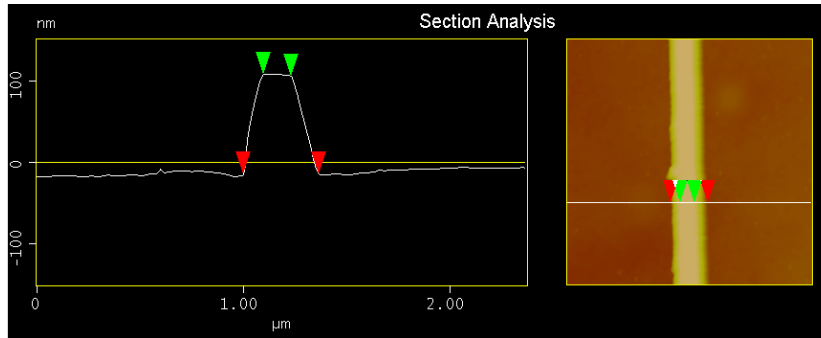
Figure 2.5: Cross section (left) and height image (right) of a SiNW, measured by AFM. The cross section was determined along the horizontal white line in the height image. This SiNW, that was patterned by writing a 125 nm wide rectangle by using e-beam lithography, has a width between 129 and 136 nm at the top (green markers) and around 360 nm at the bottom (red markers). The height is around 120 nm.

2.1.5 Contacts

The silicon nanowires were contacted by defining 150 x 200 μm sized rectangles at the end of each SiNW lead by means of UV lithography (Figure 2.2). Buffered HF was used to completely remove the top oxide in these areas. The photoresist acted as etch mask. 100 nm of aluminum were then deposited directly onto the device layer by evaporation. In order reach a low contact resistance, the evaporation rate was set to a high value (around 1 nm/s), which reduces the amount of Al_2O_3 formed in the deposited layer. Ohmic contacts were obtained by annealing the sample in forming gas at 450° C.
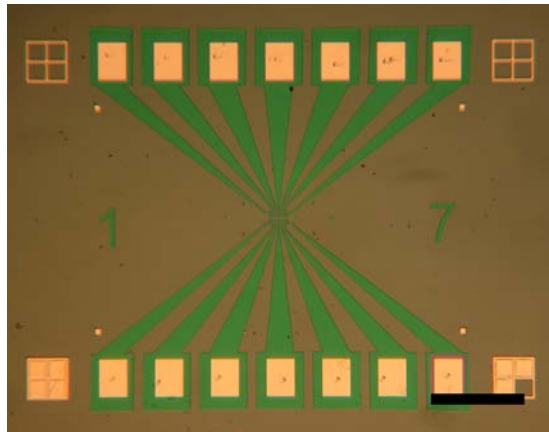
Figure 2.6: Optical Micrograph of a contacted SiNW sample. Aluminum structures such as the contact pads and alignment crosses have a yellow color, the top oxide on leads and nanowires is green. The scale bar represents 500 μm.

2.1.6 Packaging

The sample was glued on a chip carrier and the SiNWs as well as the back gate were bonded to the pins of the carrier. In order to allow measurements in liquids, these bonds and the aluminum contact pads were sealed by insulating epoxy (Figure 2.7). The epoxy was then left to dry over night at room temperature.

Figure 2.7: Photograph of a packaged SiNW sample: The sample is glued on a chip carrier and the nanowires are bonded to the pins of the carrier. In order to allow measurements in liquids, all metallic parts are sealed with an insulating transparent epoxy.

Chapter 3

Theoretical Background

In this chapter, the theoretical concepts behind the sensing mechanisms of SiNWs will be shortly described. For more details and derivations of the presented equations the reader is kindly requested to consult additional literature. Most of the below mentioned topics are covered by standard literature about semiconductor devices [34, 35], inorganic chemistry [36] and electrochemistry [37].

3.1 Silicon Nanowire field effect transistors

SiNWs that are based on SOI wafers, such as the ones used during this project (Section 2.1), can be described by metal-oxide-silicon field effect transistor (MOSFET) theory. In the following, this theory will be presented specifically for the p-doped SiNWs used during this project. In order to use SiNWs as field effect transistors, an AC voltage is applied between the two metallic contact pads, which are connected to the two ends of the nanowire via the leads (Figure 3.1). These two metallic contacts act as source and drain electrodes. The voltage applied between them is therefore called the source-drain voltage V_{SD}. The silicon substrate, which is insulated by the buried oxide layer, acts as back-gate. By altering the voltage of this back-gate, V_{BG}, the charge carrier concentration within the SiNW is influenced by electrostatic interactions. The current through the nanowire is measured by a lock-in amplifier (not shown in the figure).

3.1.1 Transfer Characteristics in air

One of the most common measurement techniques to characterize a transistor is to sweep the back-gate potential while keeping V_{SD} constant. The current that flows through the SiNW between source and drain is then plotted versus V_{BG}. Such a measurement is called the *transfer characteristics* of a transistor. In this section, these characteristics will be discussed for a p-doped nanowire in air. A plot of SiNW transfer characteristics in air is shown in Figure 3.2. This graph can be divided into several regions: Accumulation, depletion, weak and strong inversion.
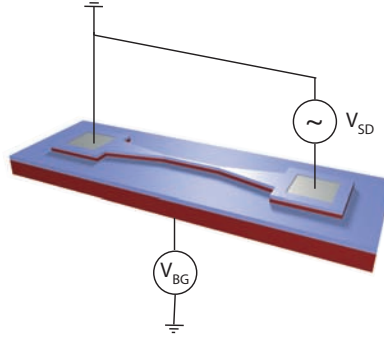
Figure 3.1: Schematic of a SiNW FET: An AC voltage is applied between the metallic contact pads that are connected with the ends of the nanowire by the two leads. These contacts act as source and drain electrode, hence the potential difference between them is denoted as V_{SD}. The silicon substrate is insulated from the nanowire by the buried oxide layer. It is used as back-gate: Depending on the voltage applied at the back-gate, V_{BG}, the charge carrier density in the silicon nanowire is altered by electrostatic forces. Adapted from [20].

Figure 3.2: Transfer characteristics of a p-doped SiNW in air. The source-drain current is plotted on a linear (black) and a logarithmic scale (red). This graph can be divided in four regions: Accumulation, depletion, weak and strong inversion. The threshold voltage for accumul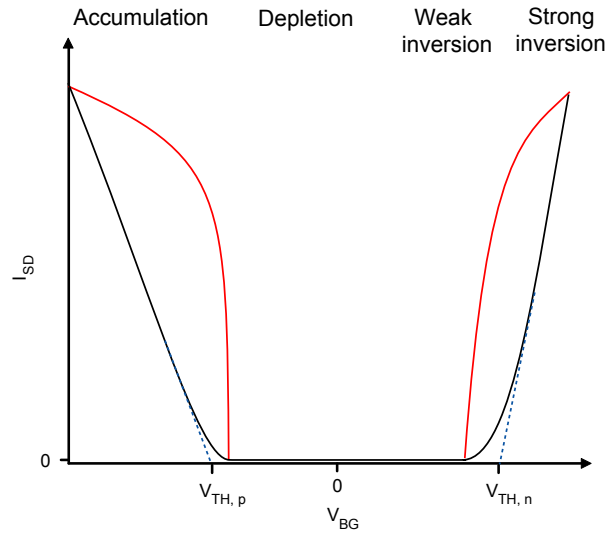ation and inversion, $V_{TH,p}$ and $V_{TH,n}$, respectively, can be determined by a linear fit, as indicated by blue dotted lines.

3.1.1.1 Accumulation

At large negative back-gate potentials, holes in the SiNW will be attracted towards its interface with the buried oxide layer and a thin layer of accumulated holes will be formed at this interface (Figure 3.3 a). As holes may easily flow between source and drain through this accumulation layer, the conductivity of the nanowire and therefore also the current between source and drain I_{SD} is large. As the back-gate voltage is swept to less negative values, the amount of positive charges at the semiconductor-buried oxide interface will decrease until this accumulated charge equals zero at the threshold voltage for accumulation $V_{TH,p}$.

For small source drain bias (i.e. $V_{SD} < V_{BG}$) and when assuming that the device mobility of the holes $\mu_{dev,h}$ does not depend on the gate voltage, the current I_{SD} through the SiNW in accumulation is given by

$$I_{SD} = \frac{W}{L}\mu_{dev,h}C_{BOX}(V_{BG} - V_{TH,p})V_{SD} \tag{3.1}$$

with the nanowire width W and length L and the buried oxide capacitance per unit area C_{BOX}. By rewriting this equation, the mobility can be extracted by plotting the conductance $G = I_{SD}/V_{SD}$ versus the back-gate voltage:

$$\mu_{dev,h} = \frac{1}{C_{BOX}}\frac{L}{W}\frac{dG}{dV_{BG}} \tag{3.2}$$

$V_{TH,p}$ is influenced by charges that are located between the semiconductor and the gate or charges that are generally in close proximity to the semiconductor surface and influence the charge carrier density in the SiNW by capacitive coupling. These charges could be either trapped charges at the semiconductor-oxide interface, charges within the oxide and finally charges on the surface of the native oxide on the side walls of the SiNWs. The latter influence on the threshold voltage is the basis of the sensing capability of SiNWs. This sensing capability can be quantified using the screening length $L_{D,Si}$ within the SiNW. In case of p-doped silicon, it is given by

$$L_{D,Si} = \sqrt{\frac{\varepsilon_{Si}\varepsilon_0 kT}{e^2 N_a}} \tag{3.3}$$

with the Boltzmann constant k, temperature T, acceptor density N_a, the elementary charge e and the vacuum permittivity ε_0. At room temperature the relative permittivity of Si ε_{Si} equals 11.7 at 1 kHz. With a doping density of $10^{15} - 10^{16}$ cm^{-3}, this screening length is between 40 and 130 nm. This length is similar to the width and height of the SiNWs and therefore charges on the side walls will reach throughout the nanowire and influence its conductivity.

3.1.1.2 Depletion

When the gate bias is swept further, the holes start to be repelled from the semiconductor-insulator interface (Figure 3.3 b). As the negatively charged acceptor ions are not mobile like holes or electrons, this results in a negatively charged layer. Because these
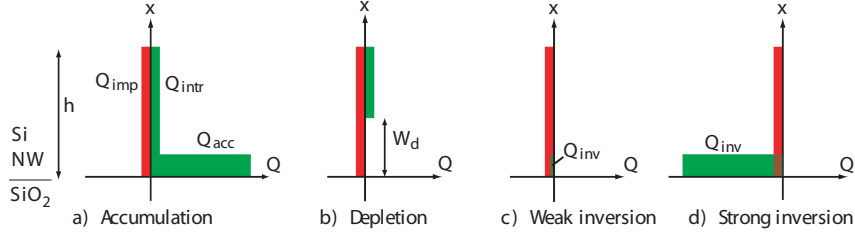
Figure 3.3: Charges within the SiNW of height h. The ordinate indicates the distance from the buried oxide. Charges left of the ordinate are negative, on the right-hand side they are positive. The red color symbolizes immobile charges Q_{imp} due to the acceptor ions. Green areas denote mobile charges. They depend on V_{BG}. a) In accumulation, a thin layer of holes with total charge Q_{acc} accumulates at the oxide-semiconductor interface. At the same time, the intrinsic hole charge Q_{intr} is present. Q_{acc} decreases with increasing V_{BG}. At $V_{TH,p}$ finally, Q_{acc} equals zero. b) In depletion, a region with a width of W_d is depleted of mobile charge carriers. c, d) As V_{BG} is increased further, electrons are attracted towards the oxide-semiconductor interface. In weak inversion, their charge Q_{inv} is still smaller than Q_{imp}. Schematics adapted from [20].

immobile charges do not contribute to the current, this layer is depleted of charge carriers and this layer therefore has a high resistance. Unlike the accumulation layer that is very thin, this depletion layer reaches into the semiconductor with a depletion width W_d. When the depletion layer is assumed to have a box profile, the maximal depletion width is approximately given by

$$W_d \approx \sqrt{\frac{\varepsilon_{Si}\varepsilon_0 E_g}{e N_a}} \tag{3.4}$$

with $N_a = 10^{15} - 10^{16}$ cm^{-3}, $\varepsilon_{Si} = 11.7$ and the silicon band gap energy, $E_g = 1.12$ eV, $W_{d,max} \approx 200 - 900$ nm. These values are well above the height of the SiNW of 70 nm. Therefore the whole nanowire is depleted, which leads to a very low I_{SD}. This is in contrast to traditional MOSFETs that have a much thicker semiconductor layer, which is only partially depleted and therefore require a n-p-n junction in order to completely turn the transistor off.

Even though in depletion the nanowire is depleted of mobile charge carriers, thermally activated charges give rise to a small so-called subthreshold current at voltages just above $V_{TH,p}$. The subthreshold swing in the depletion regime S_D is defined as the back-gate voltage change that is needed to suppress this current by one order of magnitude:

$$S_D = \frac{dV_{BG}}{d(\log_{10}(I_{SD}))} \tag{3.5}$$

S_D increases with increasing density of trap states at the oxide-semiconductor interfaces. Smaller S_D are desired as they mean a faster suppression of the I_{SD} and a lower trap state density.

13

3.1.1.3 Inversion

When the back-gate voltage reaches higher positive values, electrons start to accumulate at the semiconductor-insulator interface (Figure 3.3 c and d). As the majority charge carriers in p-type semiconductors are holes, this situation is called inversion. This inversion layer is rich in electrons and therefore a good conductor. Inversion is divided into weak and strong inversion. Strong inversion sets in as the gate voltage reaches the threshold voltage for inversion $V_{TH,n}$. Like $V_{TH,p}$, the threshold voltage for inversion is influenced by charges present in the vicinity of the semiconductor.

As in depletion, in weak inversion thermally activated charges can cause a small current just below $V_{TH,n}$. The subthreshold swing in weak inversion S_{WI} is defined analogue to S_D.

The source-drain current of the strong inversion regime can be described by the same equations as the current in the accumulation regime, but with electrons instead of holes as charge carriers. Therefore I_{SD} for small V_{SD} is given by

$$I_{SD} = \frac{W}{L} \mu_{dev,e} C_{BOX} (V_{BG} - V_{TH,n}) V_{SD} \tag{3.6}$$

with the device mobility for electrons $\mu_{dev,e}$.

3.1.2 Semiconductor and oxide capacitance

The voltage applied at the back-gate partially drops in the semiconducting substrate layer, the buried oxide and in the nanowire:

$$V_{BG} = \psi_{Sub} + \psi_{BOX} + \psi_{NW} \tag{3.7}$$

The back-gate capacitance C_{BG} is therefore given by the serial capacitance of these three layers.

$$C_{BG}^{-1} = C_{Sub}^{-1} + C_{BOX}^{-1} + C_{NW}^{-1} \tag{3.8}$$

In order to determine C_{BOX}, the geometry of the SiNW has to be considered as the field lines enter the nanowire through its interface with the buried oxide as well as through the side walls. The first component can be described as plate capacitor with a plate separation of the oxide thickness $C_{BOX,perp} = \varepsilon_{SiO_2}\varepsilon_0 / d_{BOX}$. To account for the field lines through the side walls, a correction factor $\varepsilon_{SiO_2}^{eff} \approx \varepsilon_{SiO_2}/2$ has to be introduced when the nanowire is surrounded by air [20, 38]. For a 150 nm thick buried oxide layer, this results in a capacitance $C_{BOX,air}$ of $1.2 \cdot 10^{-4}$ F/m^2 .

The two semiconductor capacitances C_{Sub} and C_{NW} when substrate and SiNW are in depletion can be described by the plate capacitance $C_{d,Sub} = \varepsilon_{Si}\varepsilon_0 / W_{d,Sub}$ and $C_{d,NW} = \varepsilon_{Si}\varepsilon_0 / W_{d,NW}$. Of course the depletion width in the nanowire is limited to its height. If the semiconductor layers are driven into depletion, they show the smallest capacitances and therefore contribute the most to the total gate capacitance. In accumulation and strong inversion there is a dense layer of charge carriers close to the semiconductor-oxide interface. Therefore W_d goes to zero and the total gate capacitance is approximately equal to C_{BOX}.

3.2 Acids and bases

In aqueous solutions (i.e. with water acting as solvent), water molecules will spontaneously disassociate to ionic species :

$$H_2O \rightleftharpoons OH^- + H^+ \tag{3.9}$$

At room temperature, this reversible reaction will lead to the equilibrium ion concentrations given by

$$[OH^-][H^+] = 10^{-14} \tag{3.10}$$

Where the brackets $[\ldots]$ denote the concentration of a chemical compound in $\frac{mol}{L}$. Usually these units are abbreviated as M. As these concentrations can vary several orders of magnitude, it is common to use their logarithms

$$-log_{10}([OH^-][H^+]) = pOH + pH = 14 \tag{3.11}$$

The pH in Eq. 3.11 is used to generally describe the acidity of aqueous solutions. At pH values from 0 to 7, the solution is acidic as $[H^+] > [OH^-]$. At pH 7 it is neutral as $[OH^-]$ equals $[H^+]$. At pH values from 7 to 14, OH^- ions dominate and the solution is basic. Generally, compounds that are able to donate H^+ ions and therefore decrease the pH are called acids, whereas bases are able to accept H^+ ions and therefore increase the pH. The acidity of a compound is given by its pK_a value which is defined as the negative common logarithm of the equilibrium constant K_a of the disassociation reaction of an acid HA to its conjugated base A^-:
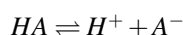
$$HA \rightleftharpoons H^+ + A^-$$

$$K_a = \frac{[H^+][A^-]}{[HA]} \tag{3.12}$$

The pH of a solution containing an acid and its conjugated base is then given by

$$pH = pK_a + log_{10}\frac{[A^-]}{[HA]} \tag{3.13}$$

Eq. 3.13 is useful when a solution is required that shows a stable pH value. Such a solution usually consists of a weak acid and its conjugated base. Weak means that not all acid molecules will disprotonate when dissolved in water. Upon addition of small quantities of bases or acids to such a solution, the equilibrium in Eq. 3.13 will be restored by disprotonation of the weak acid molecules or by protonation of the conjugated base, respectively. This way the pH value of such a solution will not significantly change. Such solutions are therefore called pH buffer solutions. The buffer is most effective when the concentrations of weak acid and its conjugated base are equal and thus $pH = pK_a$. As a rule of thumb, a buffer solution can be used in a pH range from $pH = pK_a \pm 1$.

3.3 Surface charges in electrolytes

Polar solvents, such as water, have the ability to break ionic bonds and dissolve ions. Such solutions are called electrolytes. Because of their charge, the ions will be surrounded by polar solvent molecules. This aggregation shields the electrostatic potentials between the ions and allows free motion in the solution, which leads to their ability to conduct electric current. In this section, potentials in aqueous solutions will be discussed, as these are the most commonly used electrolytes.

If a potential is applied to a solid state body immersed into an electrolyte, ions of the opposite charge will be attracted towards its surface and screen the charges of the solid state body. As the ions are still aggregated with water molecules, they form a relatively thick layer. The thickness of this so-called Gouy-Chapman double layer equals the Debye length λ_D, which is given by

$$\lambda_D = \sqrt{\frac{kT\varepsilon_r\varepsilon_0}{2N_A e^2 I}} \qquad (3.14)$$

where N_A denotes Avogadro's number and ε_r the relative permittivity of the electrolyte.

The ionic strength I of a solution is defined as the sum of the squared charge z times the concentration c of all ionic species present in the solution: $I = \frac{1}{2}\sum_i z_i^2 c_i$. The capacitance of the double layer is approximately given by

$$C_{DL} \approx \frac{\varepsilon_r\varepsilon_0}{\lambda_D} \qquad (3.15)$$

The potential drop across such an electrolyte-solid state interface is shown in Figure 3.4 a: As the ions cannot approach the surface closer than the radius of the ion-water-aggregate, there will be a small layer which is depleted of any ionic charge. This gives rise to a constant capacitance of about 0.2 F/m^2 [6] and thus a linear potential drop within this layer. The distance of closest approach is called the outer Helmholtz plane (OHP). The potential drop across the Gouy-Chapman double layer can be modeled using the Poisson-Boltzmann equation. This so-called Gouy-Chapman-Stern model is a commonly used approximation. It however fails to describe effects such as the adsorption of solvents to the surface.

The above described model does only take into account electrostatic effects. Chemical reactions which cause the formation of additional charges are not accounted for. Therefore another model, the so-called site-binding model [2], has to be applied in order to describe such effects (Figure 3.4 b): H^+ and OH^- ions are the only charged species that are present between the oxide and the OHP, as they are small and not shielded by water molecules. As in bulk solution, these ions can undergo reactions with acids and bases. In case of a SiO_2 surface, there is a large quantity of unsaturated SiOH groups. These groups are amphoteric, which means they can act as acid or base, by accepting or donating a H^+ ion

$$SiOH_2^+ \rightleftharpoons SiOH + H^+$$
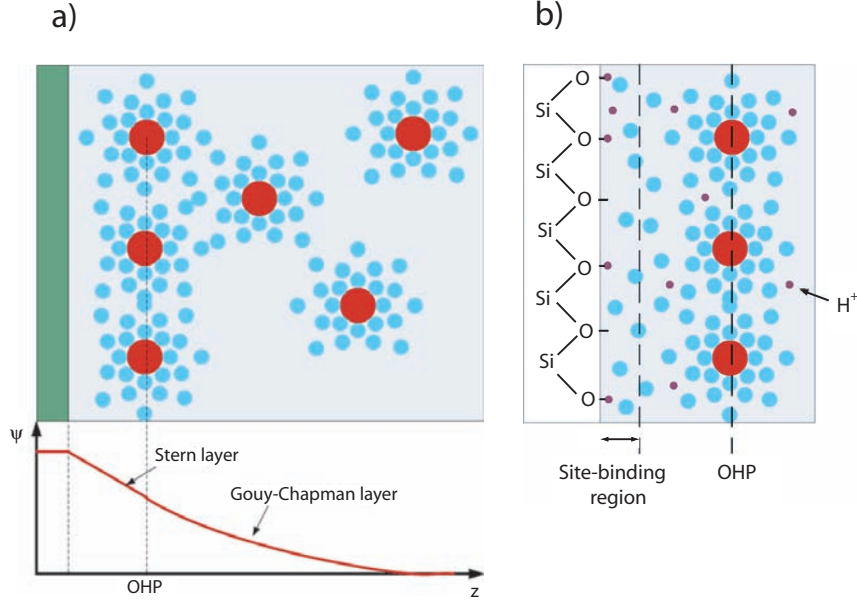$$SiOH \rightleftharpoons SiO^- + H^+$$
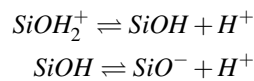
Figure 3.4: a) Dissolved ions (red) in an electrolyte in vicinity of a charged surface (green). The ions are hydrated by water molecules (blue). These aggregates are attracted to the charged surface and screen its potential. They form the so-called Gouy-Chapman layer. As the ions cannot approach the surface closer than the outer Helmholtz plane (OHP), the potential drop is linear within the Stern layer between surface and OHP. b) Site-binding model: H^+ ions may cross the OHP and bind to O^- groups of a SiO_2 surface. Adapted from: [6]

These reactions change the potential of the oxide-electrolyte interface. The maximal potential change is given by the Nernst equation

$$\Delta\psi = 2.3\frac{kT}{e}(pH_{szc} - pH) \tag{3.16}$$

Whereas the point of zero charge pH_{SZC} is the pH value at which the net surface charge is zero as the number of $SiOH_2^+$ groups equals the number of SiO^- groups. For SiO_2, $pH_{SZC} = 2$ [39].

In reality this maximal $\Delta\psi$ value of about 59 mV per pH unit at room temperature will not be reached as the surface SiO groups act as pH buffers and the concentration of H^+ ions near the surface differs from the bulk concentration [40]. In practice, SiO_2 surfaces reach a potential difference of about 30 mV/pH [2].

3.4 SiNWs in solution

SiNWs that are immersed into an electrolyte act as ion sensor due to the effects described above. During measurements in solution, an electrode immersed into the solution is used as gate additional to the back-gate. Several parameters therefore influence

the charge carrier density within the SiNW: The voltages applied at the electrode in the solution and the back-gate, ions in the vicinity of the oxide-solution interface and the charge of this oxide due to its ability to accept and donate H^+ ions.

In a typical transfer characteristics measurement in solution, the SiNW is set to ground (with a small AC voltage applied to measure the current). Therefore, the potential applied to an electrode in the solution drops across the ion double layers in the vicinity of the electrode-solution and the nanowire-solution interfaces, the top oxide or the native oxide at the sidewalls and the depletion layer within the silicon nanowire. The Back-gate potential drops over the depletion layer in the silicon substrate, the buried oxide and the depletion layer within the SiNW.

Because of the geometry of the nanowires and their small size, any charges induced from the solution-exposed side walls and the top of the nanowire may not only lead to the formation of accumulation and inversion layers near the interfaces to the top and native oxide at the side walls of the nanowire, but will also influence the charge carrier density at the interface to the buried oxide. Vice versa, the depletion layer caused by the back-gate may reach throughout the whole SiNW and therefore influences the charge carrier density near the side walls and the semiconductor-top oxide interface.

The induced charges within the nanowire by a gate electrode are proportional to the gate voltage and the capacitance over which these charges are induced. Therefore, the influence of a gate voltage on the charge carrier density in the nanowire increases with increasing capacitance.

This competition between the back-gate and the solution potentials is therefore influenced by the ratio of the different capacitances. A schematic of these capacitances is shown in Figure 3.5. Using this simplified approach, which does not take into account any influences of the back-gate on the side walls of the SiNW (assumed to be screened by the electrolyte) or charges at the oxide-solution interfaces, the total capacitances of the side walls C_S, the top C_T and the bottom C_B of the SiNW are given by

$$\frac{1}{C_B} = \frac{1}{C_{Sub}} + \frac{1}{C_{BOX}} + \frac{1}{C_{NW}} \tag{3.17}$$

$$\frac{1}{C_S} = \frac{1}{C'_{DL}} + \frac{1}{C_{NOX}} + \frac{1}{C_{NW}} \tag{3.18}$$

$$\frac{1}{C_T} = \frac{1}{C'_{DL}} + \frac{1}{C_{TOX}} + \frac{1}{C_{NW}} \tag{3.19}$$

with the total capacitance of the liquid double layer C'_{DL} (which is the capacitance of the Stern and the Gouy-Capman layer; $1/C'_{DL} = 1/C_{DL} + 1/(0.2\mathrm{Fm}^{-2})$) and the capacitances of the top oxide, the native oxide at the side walls and the buried oxide, C_{TOX}, C_{NOX} and C_{BOX}, respectively. C_{NW} and C_{Sub} denote the depletion layer capacitances of the nanowire and the silicon substrate.
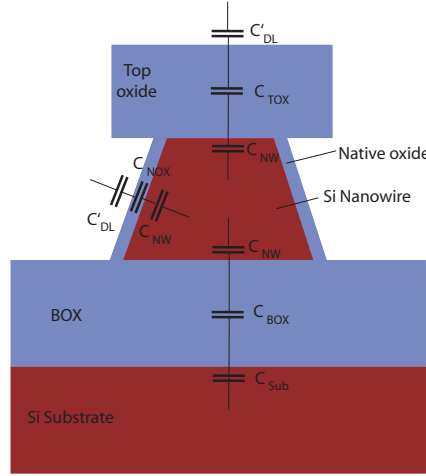
Figure 3.5: Schematic of different capacitances of a SiNW on an electrolyte. Influences of the back-gate on the nanowire side walls are neglected as well as charges of the solution-exposed oxide surfaces.

3.5 Redox reactions & Reference electrodes

Many chemical compounds undergo reactions that involve the transfer of electrons. These so-called redox reactions always involve a compound that is oxidized by donating electrons and one that is reduced by accepting electrons. Each of these two half-reactions (oxidation and reduction) has a standard potential E^0, which is defined for the case when all compounds have an activity of 1 M at 20° C and 1013 hPa. The activity a of a compound is given by its concentration times an activity coefficient γ. In an ideal solution, this coefficient equals unity. In reality, it deviates from unity with increasing concentration and temperature due to intermolecular interactions.

The potential of a half-reaction depends on the activities of the involved compounds. Usually, however, the concentration of a compound, but not its activity is known, therefore it is convenient to introduce the formal potential $E^{0'}$, which incorporates E^0 and the activity coefficients.

As potentials are always relative, E^0 is always given relative to the potential of a reference electrode. Such reference electrodes provide a stable potential, which ideally does not depend on the solution that is measured. The internationally accepted primary reference is the normal hydrogen electrode (NHE), which is a platinum electrode that is immersed into a solution with $[H^+]$=1 M. Gaseous H_2 is bubbled into this solution at a pressure of 1013 hPa. Its potential is given by the redox reaction of hydrogen to H^+. As the NHE is not easy to use, normally other reference electrodes are used, such as the calomel electrode. It obtains its potential from the reaction of mercury and chlorine in a saturated KCl ($\sim$ 4.5 M) solution:

$$Hg_2Cl_{2(electrode)} \rightleftharpoons Hg^{2+}_{2(solution)} + 2Cl^-_{(solution)} \tag{3.20}$$

19
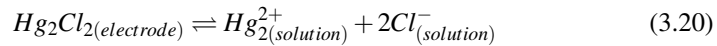
At 20° C, the calomel electrode has a potential of 242 mV vs. NHE.

In order to obtain a stable potential, the concentrations of all compound involved in the redox reactions have to be constant. Therefore the solution that is in direct contact to the Hg_2Cl_2 is saturated with KCl. The reservoir containing this solution is part of the reference electrode and separated by the analyte solution by a porous junction. This junction allows ionic conduction between the two solutions, but does not allow appreciable contamination of the analyte solution by the reference electrode solution.

A second type of reference electrodes, mostly based on noble metals, lacks this integrated solution container. The quasi-reference electrode (QRE) is therefore in direct contact with the analyte solution. The stability of such QRE is usually acceptable for short measurements, but not guaranteed on a longer term.

3.5.1 Cyclic voltammetry

A commonly used method to determine $E^{0'}$ of a compound is cyclic voltammetry:

In a typical cyclic voltammetry experiment, three different electrodes are brought in contact with the solution that is being tested: A working, a counter and a reference electrode. The working and the counter electrodes should be as inert as possible to prevent unwanted side reactions of compounds in the solution with the electrodes. Therefore materials as platinum and glassy carbon are commonly used.

A measurement is done by sweeping the working electrode potential with respect to the reference electrode, using a potentiostat with feedback loop. By this potentiostat, the counter electrode potential is driven to the potential required to establish the desired working electrode potential. During this sweep, redox-active compound in the measured solution will exchange electrons with the electrodes if their reductions or oxidation potentials are reached. As the reference potential is fed into the potentiostat over a high-ohmic input, the majority of the resulting current will flow between working and counter electrode. A reverse sweep is performed as soon as the initial sweep ends (Figure 3.6 a). During these sweeps, the current through the working electrode is measured (Figure 3.6 b).

Let's assume, only a single compound is present in the analyte. The compound can exist in its reduced form R and the oxidized form O^+. The corresponding reaction is

$$O^+ + e^- \rightleftharpoons R \tag{3.21}$$

Initially only the reduced form R is present in the solution. The measurement starts at a low potential on the left edge of the cyclovoltammogram. As the potential is increased and reaches the vicinity of $E^{0'}$ of the compound, R will be oxidized to O^+. This results in a anionic current (negative in this graph) as electrons flow from the redox-reactive compound to the anode. A reduction would cause a cationic and hence positive current. As the potential is swept over $E^{0'}$, this current increases. As the oxidation of R continues, a layer with a lower [R] near the working electrode will form. At some point, [R] at the electrode surface will be very small, so that the diffusion is the rate determining factor. This leads to a decrease of the current if the diffusion of fresh R into this layer is slower than the electron transfer: A peak occurs.
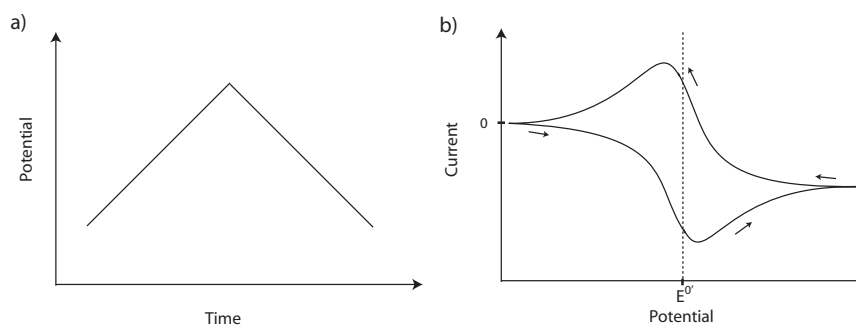
Figure 3.6: a) Working electrode potential during a cyclic voltammetry measurement. b) Cyclic voltammogram of a compound, for details see text.

When the scan direction is changed and the potential starts to decrease, [R] at the electrode surface will be virtually zero and $[O^+]$ therefore equals the bulk concentration of the compound. Therefore, the reverse sweep looks similar to the forward scan, only this time the currents are cationic and caused by reduction of O^+.

The separation of the two current peaks ideally equals $2.3kT/e$ per transferred electron. This equals about 59 mV at 25° C.

Chapter 4

Measurement set-up

During this project, the measurement set-up was gradually improved. The different versions of the set-up to measure SiNWs in air and in solution will be presented in this section, as well as the set-up that was used for cyclic voltammetry experiments and the solutions that were used to measure SiNWs.

4.1   Measurements in Air

In order to measure the conductance of a single SiNWs in air, a digital Stanford Research Systems SR830 DSP lock-in amplifier, remotely controlled by a PC was used. A LabVIEW program was used to sweep the potential of the silicon substrate of the sample (also referred to as the back-gate), while the current through the SiNW was recorded. For this purpose, the internal IV converter of the lock-in with a gain of 10^6 was connected to one contact of the nanowire (which is therefore on virtual ground), while an AC voltage of 10 mV was applied to the other contact. A DC bias was not applied between the contacts. Back-gate potentials versus ground were applied by an auxiliary out channel of the lock-in amplifier. During some measurements, the maximal potential of $\pm$ 10.5 V available at these outputs was not sufficient and an additional amplifier was used to reach voltages up to $\pm$ 100 V. In order to prevent high back-gate leakage currents, a 100 MΩ resistor was inserted between the lock-in amplifier and the back-gate.

Different AC frequencies and lock-in time constants were examined. Time constants between 10 ms and 30 ms were found to be reasonable small to allow fast measurements but also large enough to obtain a proper signal. The acquisition rate usually was set 10 times smaller than the reciprocal of the lock-in time constant. As the capacitive current between back-gate and SiNW increases with increasing AC frequency (Figure 4.1 a), the lowest frequency that still showed a low noise level was chosen. The AC frequency was therefore usually set to 131 Hz or 317 Hz (Figure 4.1 b).

This set-up only allowed the measurement of a single SiNW. Comparing different SiNWs on a sample therefore was only possible by serially measuring the individual wires. In order to allow the measurements of up to eight SiNWs in parallel, two multiplexer were inserted between the lock-in signal output and the SiNWs and between
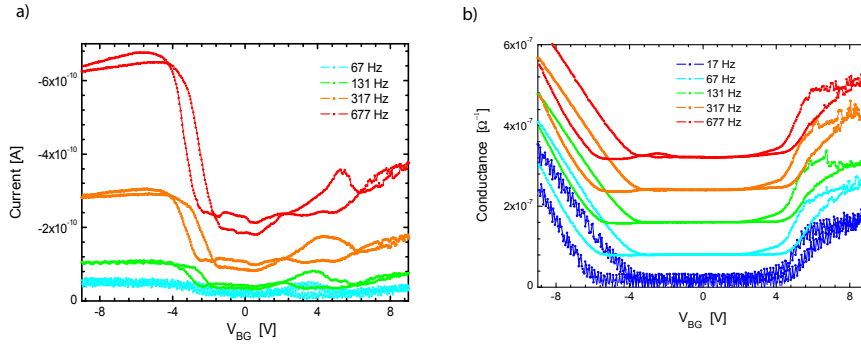
Figure 4.1: a) The capacitive part (i.e. the Y-component of the lock-in output) of the current through a 100 nm wide and 10 μm long SiNW in air. It linearly increases with increasing AC frequency. The lock-in time constant was set to 10 ms, the acquisition rate was 10 Hz. b) Transfer characteristics of the same SiNW at different AC frequencies. The curves are shifted for clarity. The lock-in time constant was set to 10 ms, the acquisition rate was 10 Hz. The noise level decreases until a AC frequency of 131 Hz and then remains constant. Except for the noise, the measured conductance curves are not significantly influenced by changes in the AC frequency.

the nanowires and the signal input of the lock-in (Figure 4.2). As the SiNWs were now temporary disconnected from the lock-in amplifier, a capacitive current caused by the buried oxide layer capacitance was measured upon switching between the wires. In order to avoid any interference with the measurement or damage of the sample, the drain of each SiNW was permanently connected to the ground over a 1 MΩ resistance. As the Lock-in signal input to the internal IV converter is low-ohmic (about 1 kΩ), this parallel high-ohmic connection to the ground should not significantly interfere with the measurement, but allow the capacitive current to flow to the ground while the SiNW is not connected to the lock-in. Control measurements in air conducted using the multiplexers confirmed that the results were not significantly influenced (Figure 4.3).

4.2 Measurements in Liquids

Measurements in liquid were performed using the same set-up as the measurements in air with additional components. A liquid cell (home-built by the mechanics workshop) containing a platinum electrode and a reference electrode was placed on top of the chip carrier (Figure 4.4), such that the whole SiNW sample was covered by liquid. This cell had a volume of about 0.2 ml. By a remotely controlled pump, liquid could be transferred from a glass flask that contained the measured solution to this liquid cell. During all measurements, inert N_2 gas was led into this flask in order to replace dissolved oxygen.

During initial measurements the Pt electrode potential was directly swept while recording the potential of the SiNW relative to the potential of the reference electrode. A silver wire, that was directly immersed into the solution, was used as quasi-reference electrode.
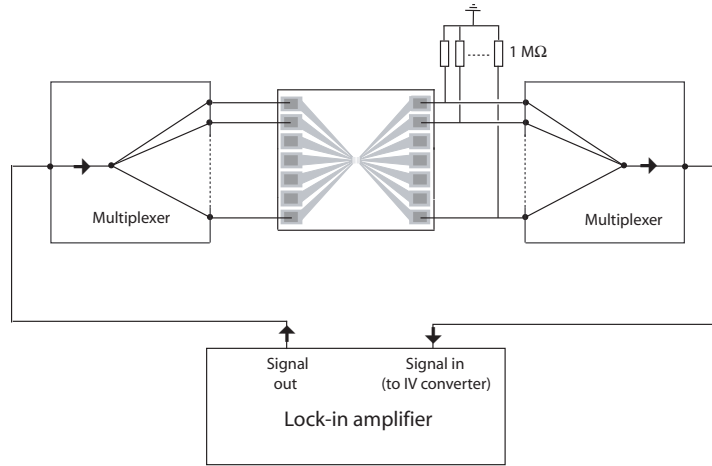
Figure 4.2: Schematic of the set-up to measure up to eight SiNWs in parallel. The lock-in AC signal is selectively applied to an individual nanowire by the left multiplexer. The other SiNW contact is constantly connected to ground over a 1 MΩ resistance. This is necessary as otherwise charges may accumulate due to the capacitance between the SiNW and the back-gate while the nanowire is not connected to the lock-in by the multiplexer. A second multiplexer finally collects the current through the nanowire and leads it to the internal IV converter of the lock-in amplifier. Both multiplexer are always switched simultaneously to the same nanowire.

Figure 4.3: Transfer characteristics of a 100 nm wide and 10 μm long SiNW in air. There is no significant difference visible between measurements conducted using multiplexers and measurements without multiplexers. The lock-in time constant was set to 10 ms, the acquisition rate was 10 Hz. The AC frequency was set to 317 Hz.

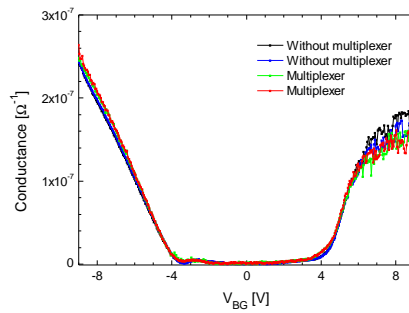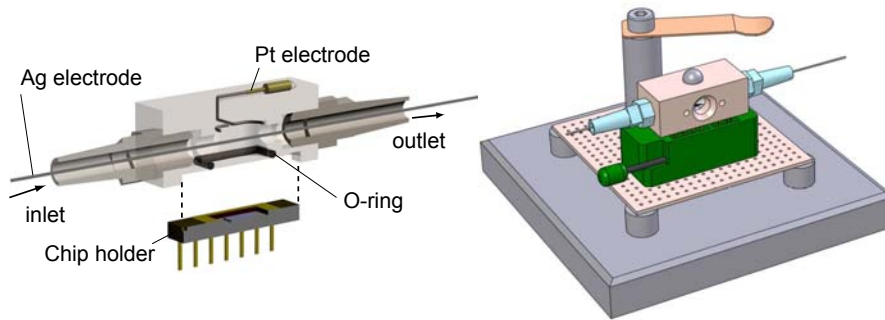Figure 4.4: Left: Schematic of the liquid cell with a silver wire as reference electrode. An O-ring ensures a tight connection between chip holder and the liquid cell. Right: The liquid cell is pressed on the chip holder containing the SiNW sample by a metal clamp. In this image, the hole in the liquid cell side wall to insert the calomel reference electrode is visible.

A more sophisticated set-up was then constructed during this project: A potentiostat (home-built by the electronics workshop) was used to control the potentials of the different electrodes. Instead of the Ag wire, a calomel reference electrode in saturated KCl was used (Section 3.5).

A typical measurement was conducted by sweeping the set-point of the potential difference between the SiNW and the calomel electrode using a LabVIEW program that was written during this project. The potentiostat compared this set-point with the actual potential difference between calomel reference electrode and SiNW and altered the voltage applied at the Pt electrode until the set-point was reached (Figure 4.5, additional information is provided in the appendix). The reference potential input of the potentiostat was very high ohmic in order to keep the current through the reference electrode small. During this potential sweep, the back-gate voltage was kept constant versus ground. Usually a measurement consisted of several such sweeps at different back-gate voltages. Between two sweeps, solution was pumped through the liquid cell for 20 s with a flow rate of about 1 ml per minute. The current through the SiNWs, the voltage applied at the platinum electrode as well as the current flowing through it and the difference between the set-point and the actual potential difference between the SiNW and the reference electrode were monitored during these sweeps. Except for the SiNW conductance, all data that was collected was transmitted via the auxiliary ports of the lock-in amplifier.

In order to protect the sample, the maximal current through the platinum electrode could be limited to either $1\mu A$, $10\,\mu A$ or 10 mA. SiNWs were measured using the first two modes, the last mode was used to conduct cyclic voltammetry experiments.

The feedback loop of the potentiostat could be adjusted to a bandwidth between 0.1 Hz and 1kHz. For all solution measurements, an acquisition rate of 3.33 Hz was chosen and the potentiostat's feedback loop bandwidth was set to 30 Hz. At this conditions, the error between the set-point and the actual potential difference between the SiNW and the reference electrode was usually smaller than 1 mV. These 30 Hz are also slow enough to average out any possible potential fluctuations caused by the AC current through the SiNWs, which was usually set to 131 Hz.
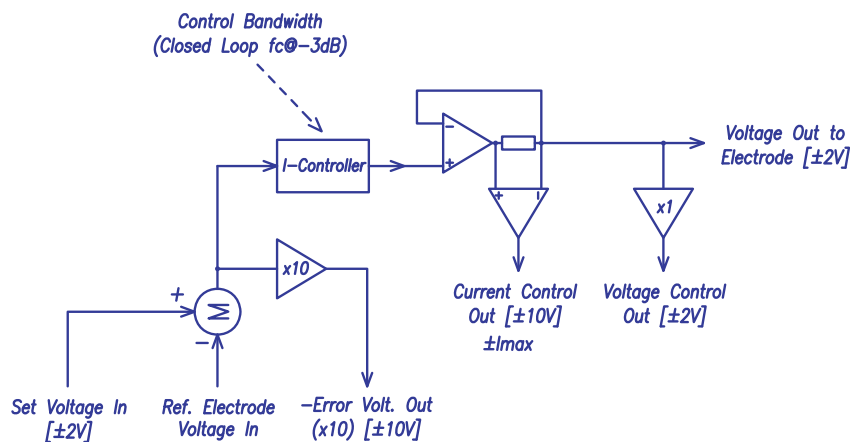
Figure 4.5: Schematic of the potentiostat: The voltage applied to the platinum electrode is altered until the difference between the SiNW and the reference electrode potential equals the set-point. The bandwidth of the feedback loop can be adjusted from 0.1 Hz to 1 kHz. The potential applied to the Pt electrode as well as the current that flows through it can be monitored during the measurement. The feedback loop can remotely be turned off by a TTL signal (not shown in schematic). The current through the Pt electrode can be limited to either 1 μA, 10 μA or 10 mA.

4.3 Cyclic voltammetry set-up

Another set-up was used to conduct cyclic voltammetry experiments in order to test the stability of reference electrodes. A solution containing a redox-active compound was given into a liquid container with a volume of about 5 ml. A platinum electrode was used as counter electrode, a rod of glassy carbon as working electrode. These two electrodes as well as the calomel reference electrode were connected to the potentiostat described above. A LabVIEW program was used to sweep the potential of the working electrode with respect to the reference electrode by applying the necessary potential at the counter electrode. During such a sweep, the current through the working electrode was recorded. N_2 gas was led directly into the liquid cell to replace dissolved oxygen.

4.4 Measurement solutions

Additionally to the measurement set-ups, the solutions in which the sensor capabilities of SiNWs were examined shall be shortly presented and discussed.

4.4.1 Dilution series

In order to measure the influence of the ion concentration on the SiNW conductance, two different dilution series were prepared. The first dilution series comprised different concentrations of Dulbecco's Phosphate Buffered Saline (DPBS). The undiluted DPBS is an aqueous solution containing 137 mM NaCl, 8 mM Na_2PO_4, 2.7 mM KCl and 1.4

26

mM KH_2PO_4 (or 8 g/L NaCl, 1.15 g/L Na_2PO_4, 0.2 g/L KCl and 0.2 g/L KH_2PO_4). This results in an ionic strength of 168 mM. The series was then prepared by recursively diluting the solution six times by a factor of ten. These solutions will in the following be named 10^{-y} x DPBS, where 10^{-y} denotes the dilution factor compared to the initial DPBS concentration. The pH values of these solutions varied between 7.0 and 5.8 for 1 x DPBS and 10^{-6} x DPBS, respectively. The deionized water that was used to prepare the solutions had a pH of 5.9. The pH only remained relatively constant down to 10^{-2} x DPBS. Further dilution measurements were therefore conducted using a series of aqueous KCl solutions with concentrations between 1 M and 10 μM, which could be prepared more easily but did not have a pH buffer capability.

4.4.2 pH-buffer series

The pH of aqueous KCl and KOH solutions is not stable as those compound are not able to compensate fluctuations of H^+ or OH^- ions, which can be caused by chemical reactions or dissolved gases in the solution. Solutions whose pH was adjusted by only using KCl and KOH with concentrations around 10 mM had been used during previous SiNW measurements [20, 30]. The pH values of such solutions were measured again several days after they had been prepared with a pH value uncertainty of ±0.05. A solution with initially a pH value of 4 showed a pH of 5.4 and a solution with an initial pH of 10 had a pH of 9.

In order to guarantee stable conditions, all pH measurements during this project were therefore conducted using pH buffer solutions. These solutions were prepared according to Table 4.1. As an acid-base pair usually covers a range of about 2 pH values, three different buffering compound were used. The ratio between the acid and its conjugated base of the buffering compound (and therefore also the pH of the solution) was adjusted by adding 100 mM KOH or 100 mM HCl until the pH reached the desired value with an uncertainty of ±0.05.

pH	buffer	[buffer] [mMol/L]	[HCl] [mMol/L]	[KOH] [mMol/L]
3	KH phthalate	41	18	-
4	KH phthalate	50	-	-
5	KH phthalate	41	-	18
6	KH_2PO_4	47	-	5
7	KH_2PO_4	39	-	22
9	$Na_2B_4O_7$	23	8	-

Table 4.1: Final concentrations of pH buffer solutions. The buffers were prepared by providing an aqueous solution containing the buffering compound and adding appropriate aliquots of HCl or KOH.

4.4.3 Cyclic voltammetry solution

The stability of the Calomel reference electrode was measured by cyclic voltammetry in an aqueous solution of 2.5 mM $Ru(NH_3)_6Cl_3$ and 500 mM KCl. The half reaction

$$Ru(NH_3)_6^{3+} + e^- \rightleftharpoons Ru(NH_3)_6^{2+} \qquad (4.1)$$
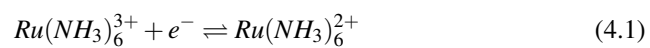
has an E^0 of 100 mV at 25° C versus NHE [37].

Chapter 5

Results & Discussion

5.1 Previously fabricated SiNWs

Silicon nanowires that had previously been fabricated according to the original fabrication protocol [20] were characterized in air and in solution. Furthermore, the sensing capabilities of these SiNWs were examined. All results presented in this section were obtained from two previously fabricated SiNWs with a length of 1 μm and 10 μm, respectively. Both nanowires were about 100 nm wide.

5.1.1 Characteristics in air

The transfer characteristics of those two SiNWs in air are shown in Figure 5.1. As they have already been presented [20], they shall only be discussed briefly .

Subthreshold swings and threshold voltages were extracted from these graphs (Table 5.1). Device mobilities for holes and electrons were calculated using the slope of the linear parts of the conductance graphs and assuming an oxide capacitance of $1.2 \cdot 10^{-4}$
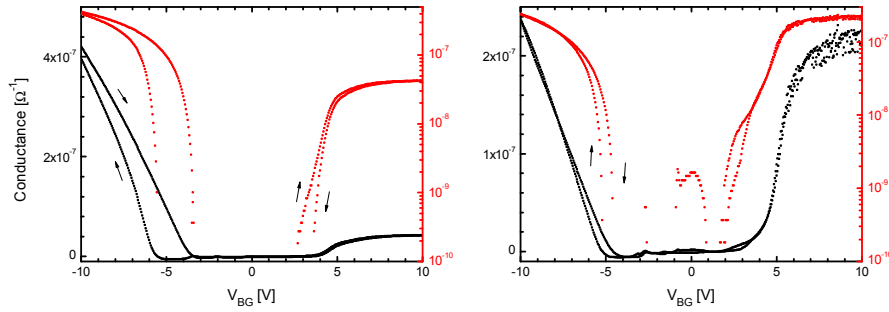

Figure 5.1: Transfer characteristics of previously fabricated nanowires with length of 1 μm (left) and 10 μm (right). They are plotted in linear (black) as well as in logarithmic (red) scale.

L [μm]	$\mu_{dev,h}$ [cm^2/Vs]	$\mu_{dev,e}$ [cm^2/Vs]	S_D [mV/dec]	S_{WI} [mV/dec]	$V_{TH,p}$ [V]	$V_{TH,n}$ [V]
1	56	18; 2	120	690	-3.4	4.1
10	388	1000	130	670	-4.8	4.3

Table 5.1: Device mobilities, subthreshold swings and threshold voltages of two previously fabricated SiNWs.

F/m^2 (Section 3.1.2). The two values for $\mu_{dev,e}$ in case of the shorter SiNW were obtained from the steeper and the flatter slope of the inversion regime, respectively.

Both device mobilities of the 10 μm long SiNW were in agreement with usually observed mobilities in the device layer of SIMOX SOI wafers [41]. The $\mu_{dev,e}/\mu_{dev,h}$ ratio of the 10 μm long SiNW was about 2.7, which is similar to the ratio of 2.9 of the drift mobilities of electrons and holes in silicon [34]. The shorter wire showed much smaller device mobilities and a ratio of about 0.3. The small ratio as well as the saturation of the inversion current are probably caused by trap states in the top oxide. It was shown [20] on similar SiNWs that at least the saturation could be eliminated by removing the top oxide. Why this issue only occurred at the shorter nanowire is unknown yet.

The fact that both device mobilities of the shorter SiNW were significantly lower than those of the longer one could be due to the calculation of these values, which involve the length of the nanowire: As soon as the SiNW gets so short, that the resistance of the leads and the contacts starts to dominate, dG/dV_{BG} becomes independent of the nanowire length. The calculated charge mobility in contrast still decreases with decreasing wire length as it does not take the leads and contact effects into account.

Both SiNWs had almost identical subthreshold swings in depletion as well as in weak inversion. They also showed similar V_{TH} values. A detailed analysis of these values was presented in [20]. In summary, the small S_D and threshold voltages are attributed to the high quality of the SOI wafer. The large S_{WI} values could be due to a Schottky barrier at the interface between the silicon device layer and the aluminum contact pads when the semiconductor is in inversion.

5.1.2 Characteristics in solution

In order to obtain SiNW characteristics in liquid, the 1 μm long nanowire was measured in aqueous solutions. The set-up comprising a potentiostat and a calomel reference electrode was used (Section 4.2). The measurement was conducted by sweeping the potential difference between the SiNW and the calomel reference electrode (will be referred to as $V_{Calomel}$) in steps of 10 mV by applying a potential at the Pt electrode. The back-gate voltage was set to values of -9,-8....9 V.

When comparing the voltage that is applied to the Pt electrode with $V_{Calomel}$ at constant back-gate voltages, a linear dependence with slope of about one is observed. This means $V_{Calomel}$ follows the voltage that is applied at the Pt electrode (Figure 5.2 a). For different back-gate voltages however, the offset between those two potentials is shifting between 100 and 900 mV. This shift can be explained by the capacitative influence of the back-gate on the solution, which has to be compensated by the platinum electrode. As the capacitance of the SiNW and the silicon substrate depends on whether they
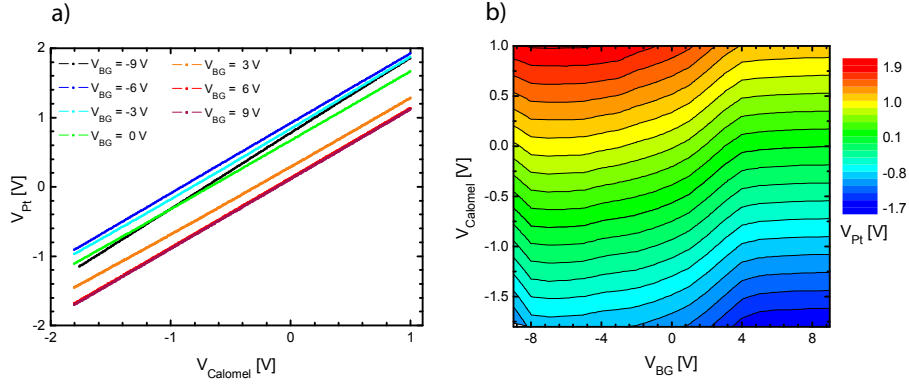
Figure 5.2: a) The platinum electrode potential linearly depends on $V_{Calomel}$ for a given V_{BG}. The offset between these two potentials varies for different V_{BG}. b) Contour plot of the dependence of V_{Pt} on $V_{Calomel}$ and V_{BG}. As already seen in the left image, V_{Pt} linearly depends on $V_{Calomel}$. The V_{BG}-dependence however is non-linear. This measurement was conducted in pH 7 buffer solution, using the 1 μm long previously fabricated SiNW.

are in depletion, accumulation or inversion, the shift between $V_{Calomel}$ and V_{Pt} shows a non-linear dependence on the back-gate voltage, as can be seen in the contour plot in Figure 5.2 b. As all contour plots presented in this report, it was created directly from the raw data using the *XYZ Contour* option in OriginLabs Origin 8.0. If not mentioned specifically, no smoothing of the contour levels was applied.

Due to this non-linear relation between V_{Pt} and $V_{Calomel}$, any slopes or characteristics of SiNW measurements in solution will appear differently, depending on whether the conductance is plotted versus V_{Pt} or $V_{Calomel}$. As the charge carrier density within the SiNW is influenced by the potential difference between the nanowire and the solution (measured by the reference electrode) and not directly by the potential of the platinum electrode, the characteristics of this SiNW in solution will be analyzed using a contour plot of the conductance versus $V_{Calomel}$ and V_{BG} (Figure 5.3). This contour plot shows two regions with a conductivity up to $4 \cdot 10^{-7}$ Ω^{-1} when V_{BG} as well as $V_{Calomel}$ are driven to negative or to positive values. If these two potentials show opposite signs, the conductance remains below 10^{-8} Ω^{-1}.

The highly conductive region at negative V_{Pt} and $V_{Calomel}$ shows a contour level kink at V_{BG} of around -4 V. On the left-hand side of this kink, the $dV_{Calomel}/dV_{BG}$ slope of equipotential lines is very small, on the right-hand side, it increases to a value of about 0.2.

More detailed information is obtained when the conductance is plotted versus the back-gate voltage for different $V_{Calomel}$ (Figure 5.4 a). In accumulation (i.e. $V_{Calomel} = -1$ and -1.5 V), the conductance linearly depends on V_{BG} until about -4 V, then it becomes much less dependent on V_{BG}. In inversion on the other hand (i.e. $V_{Calomel} = 0$, 0.5 and 1 V), the conductance linearly increases with increasing V_{BG} until 9 V and does not saturate. This is in contrast to the saturation observed in inversion during measurements in air (Figure 5.1, left image). This observation supports the assumption that those parts of the SiNW which are exposed to the liquid (e.g. the top oxide) and not contact effects are responsible for the low inversion conductance in air.
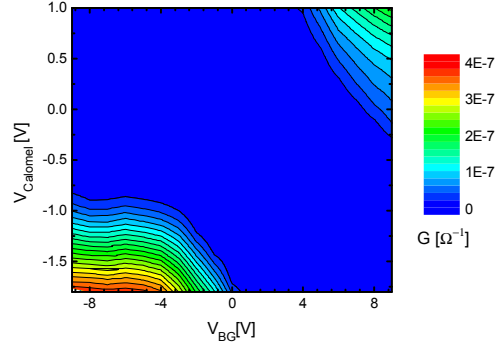
31

Figure 5.3: Contour plot of a measurement with the previously fabricated 1 μm long SiNW in 10 mM KCl solution. The conductance is plotted as colors versus V_{BG} and $V_{Calomel}$. The potential difference between the calomel reference electrode and the SiNW was swept by applying the necessary potential to a Pt electrode, using a potentiostat. The contour plot shows two highly conductive regions when both gates potentials are negative or when both are positive. In this contour plot, negative conductance values that occurred at low conducting regions due to fluctuations, were set to zero.

When the SiNW conductance is plotted versus $V_{Calomel}$ (Figure 5.4 b), two almost identical curves at $V_{BG} = -9$ V and -6 V are observed (this corresponds to the small $dV_{Calomel}/dV_{BG}$ ratios of equiconductance levels in the contour plot). This demonstrates the dominance of the platinum electrode over the back-gate in this region. $V_{TH,Calomel}$ at these back-gate voltages was around -0.8 V. At less negative back-gate voltages, $V_{TH,Calomel}$ rapidly shifts to more negative values and the slope decreases. In inversion (i.e. $V_{BG} = 6$ V and 9 V), the slope is significantly smaller than in accumulation, but similar for both back-gate voltages. In accumulation as well as in inversion, the conductance does not saturate.

A comparison of Figure 5.4 a and b shows that $dG/dV_{Calomel}$ is four to seven times larger than dG/dV_{BG}.

In order to analyze this results, the influence of both gates has to be considered: The Pt electrode as well as the back-gate are simultaneously used to influence the conductivity of the SiNW. Each of these gates is individually able to drive the SiNW into depletion, accumulation or inversion. In a hypothetical system where these two gates do not interfere, accumulation or inversion would be expected if one of these gates is set below its threshold voltage for accumulation or above its threshold voltage for inversion (Figure 5.5 a). In case of SiNWs with a width and height similar to the screening length in silicon, the back-gate as well as the Pt electrode is able to influence the charge carrier density throughout the SiNW. Therefore, accumulation and inversion are expected if the combination of $V_{Calomel}$ and V_{BG} allows these regimes (Figure 5.5 b). In this case, the $dV_{Calomel}/dV_{BG}$ slope of the equiconductance levels is proportional to the coupling efficiency of the back-gate relative to the Pt electrode. In case of a p-doped SiNW, accumulation is expected to occur towards more negative gate voltages than inversion. This model does not take into account any influences of the leads or the contacts.
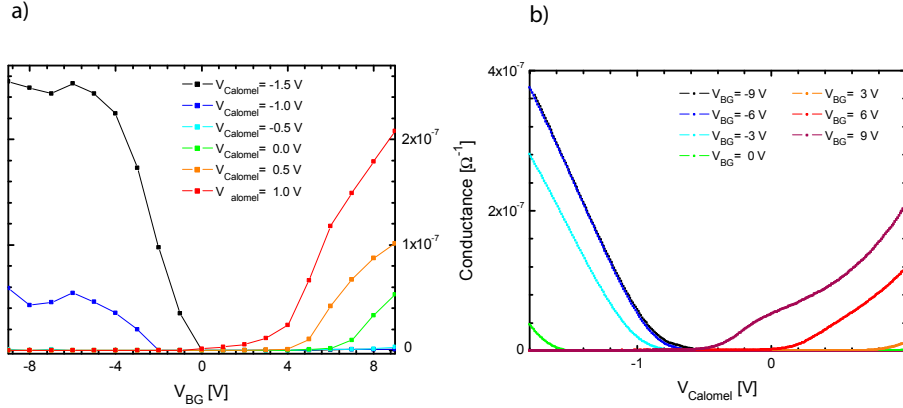
Figure 5.4: a) Conductance of the SiNW versus the back-gate voltage at different $V_{Calomel}$. For $V_{Calomel} \leq -1$ V, the nanowire is in accumulation. However, the conductance is only high if the back-gate also drives the parts of the leads that are sealed by epoxy into accumulation. The same behavior is observed in the inversion region at $V_{Calomel} \geq 0$ V. In contrast to the measurements in air, a saturation of the inversion conductance was not observed. b) The SiNW conductance versus $V_{Calomel}$ at different V_{BG} shows linear dependence in the accumulation as well as in the inversion regime. A saturation is not observed.

The measured conductance partially shows this expected behavior. However, in accumulation the $dV_{Calomel}/dV_{BG}$ slope of equipotential lines suddenly increases at a V_{BG} of around -4 V. This back-gate voltage is similar to $V_{TH,p}$ measured in air. This behavior is therefore attributed to those parts of the silicon leads that are sealed by expoy and thus are not influenced by the Pt electrode. If these parts are driven into depletion or into the opposite regime than the parts covered by the solution, the conducing charge carrier layer between source and drain contacts is interrupted by a lack of charge carriers in the first case or a p-n junction in the latter (Figure 5.5 c). This should however cause an infinitely large $dV_{Calomel}/dV_{BG}$ slope of equipotential lines, as the Pt electrode should have no influence on this effect. The measured large, but finite slope on the right-hand side of the kink indicates that the Pt electrode still has limited influence within this voltage range. A possible cause could be that the epoxy coating is not completely impermeable to the solution.

In contrast to the accumulation region, the situation is less clear in inversion. This could be due to additional influences, such as Schottky barriers at the contacts.

In summary, these measurements suggest that the analysis of solution measurements requires a stable reference potential, as the Pt electrode voltage non-linearly depends on V_{BG} and therefore can't be used to analyze SiNW characteristics in solution. Furthermore, those parts of the contacts that are sealed by epoxy strongly influence the conductance of the sample in inversion (at least within the measured potential range) as well as at those parts of the accumulation region where V_{BG} is in the range of $V_{TH,p}$ measured in air. In accumulation at V_{BG} well below $V_{TH,BG}$, the influence of the platinum electrode and therefore most probably also the conductance of the nanowire dominates.
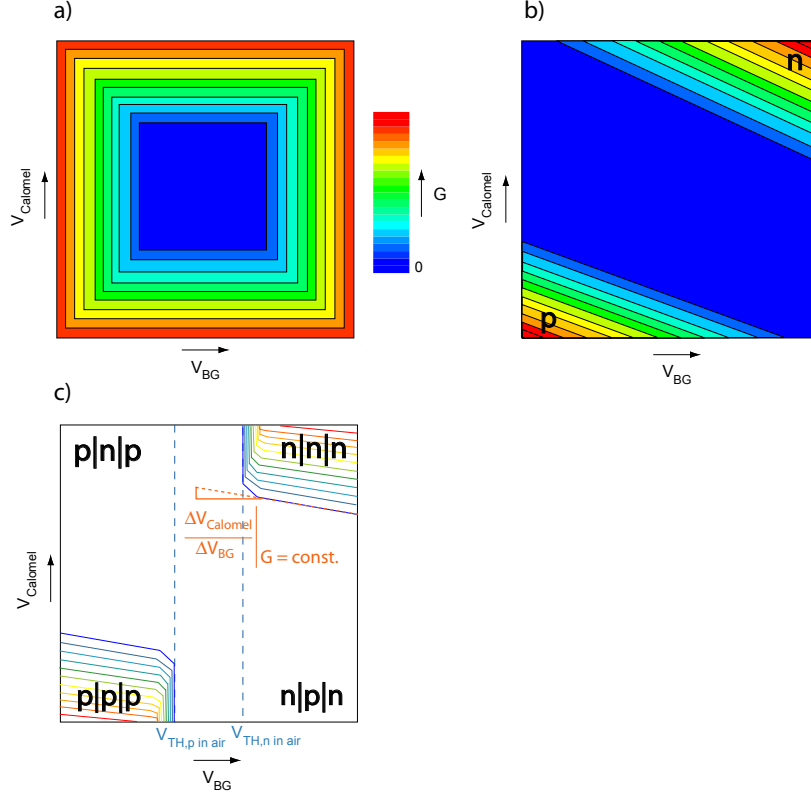
Figure 5.5: Schematics of conductance versus $V_{Calomel}$ and V_{BG} contour plots, as expected for dual-gated solution measurements of different systems: a) Contour plot in case of a system with two non-interfering gates. Accumulation and inversion are expected when one of these gates is driven below $V_{TH,p}$ or above $V_{TH,n}$. b) Expected behavior of a p-doped SiNW, without considering the role of the leads or contact effects. Accumulation (denoted by p) is expected at more negative gate voltages compared to inversion (n). c) Schematic of the expected SiNW conductance: Those parts of the silicon leads that are sealed by epoxy lead to a suppression of the current through the SiNW whenever they are driven into depletion or the opposite regime compared to the SiNW and the parts of the leads that exposed to the solution (these situations are denoted as p|n|p and n|p|n). When the leads and the SiNW are both in accumulation or inversion (p|p|p and n|n|n), a high conductance is measured. This should lead to a sudden change of the $dV_{Calomel}/dV_{BG}$ slope of equipotential levels at back-gate voltages that are similar to the threshold voltages when the SiNW is measured in air (indicated by blue dashed lines). The measured conductance corresponds to this graph in accumulation. However, although the $dV_{Calomel}/dV_{BG}$ slope of equipotential levels on the right-hand side of the kink is considerably larger than the slope on the left-hand side, it is still not nearly close to the expected infinitely steep slope. In inversion, the measured conductance differs from this graph. This could be due to influences that were not considered, such as Schottky barriers at the contacts.

5.1.3 Sensing capability of previously fabricated SiNWs

After the general SiNW characteristics in solution have been discussed, the sensing capability of these SiNWs shall be examined. Unfortunately, these previously fabricated nanowires rapidly degraded after few weeks of solution measurements, such that new SiNWs had to be fabricated soon after the modified set-up was ready to use. For this reason no systematic pH or concentration measurements could be conducted with these SiNW and the improved set-up. Therefore, earlier measurements conducted using these previously fabricated SiNWs and the initial set-up will be presented.

Such measurements were performed by directly sweeping the platinum electrode potential while measuring the potential difference between the SiNW and a silver wire (will be referred to as V_{Ag}). This set-up had a major drawback: The silver wire was directly immersed into the measured solution and acted as a quasi-reference electrode. Therefore the stability of this reference potential at a changing ion concentration or during longer measurements, where any molecules present in the solution might adsorb at the silver wire, is very questionable.

These reference potential shifts are especially problematic during pH measurements, as a pH change of the solution is expected to shift the threshold voltages relative to the reference potential. For this reason, a stable reference potential is essential. This issue was already observed during previous pH measurements that were conducted using the same set-up and that already have been presented [20]: $V_{TH,Ag}$ shifted up to around 200 mV per pH unit, which is much more than the 59 mV predicted by theory (Section 3.3). The threshold voltage sometimes even shifted in the opposite direction than theoretically expected. These results indicate that these shifts are not only due to pH changes, but probably either originate from hysteresis effects in the SiNW or from reference potential shifts.

Another limitation of this set-up is the fact that the platinum electrode potential was swept directly, which means that any graph of V_{Ag} will be an interpolation and an exact data analysis is therefore not always possible (the modified set-up does not suffer from this issue as the potential difference between the SiNW and the reference electrode is linearly swept using the potentiostat).

As mentioned above, pH measurements using the initial set-up were not very informative and therefore won't be presented again. Ion concentration measurements that were conducted using the initial set-up might give more information and therefore will be presented and analyzed, keeping the limitations of this set-up in mind.

5.1.3.1 Influence of the solution concentration

The concentration of dissolved ions is an important parameter when measuring SiNWs in solution [24, 25]. The capacitance of the ion double layer in the vicinity of the SiNW oxide surfaces increases with increasing ion concentration (Section 3.3). As the Pt electrode potential influences the charge carrier concentrations in the SiNWs via this capacitance (Section 3.4), the influence of the Pt electrode relative to the back-gate is assumed to increase with increasing ion concentration.

Moreover, in case of functionalized SiNWs, the ion concentration is crucial. Such nanowires sense the change in the electric field due to the binding of specific molecules, for example a ligand or complementary RNA. The distance between these bound molecules

and the nanowire surface is typically several nm. If λ_D is smaller than this distance, all charges of the molecule will be screened and the nanowire won't detect the binding of this molecule [24]. Therefore usually low ion concentrations are chosen for such measurements.

The $1\,\mu$m long SiNW was measured in a dilution series of DPBS. Seven solutions from undiluted (1 x) to 10^{-6} times diluted (10^{-6} x) DPBS were used. Contour plots of these measurements are presented in Figure 5.6. These measurements were conducted by sweeping the Pt electrode potential in steps of 10 mV at back-gate voltages of -9, -8 ... 2 V. The Conductance of the SiNW is plotted versus the Ag wire reference potential and the the back-gate voltage. At the chosen voltage range the accumulation region of the nanowire was measured. As described before, two different dV_{Ag}/dV_{BG} slopes of equiconductance levels were observed, with a more or less sharp kink at around $V_{Bg} = -4$ V. These two slopes were manually extracted by determining the $\Delta V_{Ag}/\Delta V_{BG}$ ratio for each DPBS concentration at a conductance of $1.5 \cdot 10^{-7}\ \Omega^{-1}$ (Table 5.2). This ratio is a measure for the relative coupling efficiency of the back-gate compared to the platinum electrode gate.

The steeper slope at the right-hand side of the kink slowly increased with decreasing concentration. The $\Delta V_{Ag}/\Delta V_{BG}$ ratio on the left-hand side of the kink showed much stronger dependence on the solution concentration between 10^{-5} to 10^{-2} x DPBS and remained almost constant at higher and lower concentrations. This slope varied between 0.12 and 0.02, which means the Pt electrode gate was between eight and fifty times as efficient as the back-gate.

In order to estimate the error induced by the Ag wire reference potential shifts, $V_{TH,Ag}$ was determined at back-gate voltages of -5, -7 and -9 V for all DPBS concentrations (Figure 5.7). $V_{TH,Ag}$ at all three back-gate voltages strongly varied, especially at higher concentrations. These shifts do not correlate to the shift of the $\Delta V_{Ag}/\Delta V_{BG}$ ratio. The ratios of the three highest concentrations for example were almost identical in contrast to the threshold voltages. Furthermore, the shifts do not seem to correlate with the solution concentration. As any baseline subtraction is therefore not possible, these shifts won't be accounted for during the analysis. A comparison with theory will show if these measurements provide any information anyhow.

In the following, the less steep dV_{Ag}/dV_{BG} slope on the left-hand side of the kink will be mainly discussed, as the steeper part is assumed to be strongly influenced by the the partially sealed leads.

In order to compare these slopes with the simple capacitance model presented in Section 3.4, the values of all involved capacitances were calculated for all solution concentrations. The double layer thickness and capacitance for each solution is shown in Table 5.2. They were calculated using equation 3.14 and 3.15, with $\varepsilon_r \approx \varepsilon_{H_2O} = 80.1$ and $I_{1xDPBS} = 168$ mM. The SiNW as well as the silicon substrate were assumed to be in accumulation with a very small depletion width, therefore their capacitances were neglected. The different oxide capacitances were calculated assuming a buried oxide thickness of 150 nm, a 3 nm thick native oxide layer and a top oxide thickness of 50 nm (the top oxide becomes thinner during the fabrication, see Section 2.1.4). The total capacitances of the top, side and bottom of the SiNW, C_T, C_S and C_B were plotted versus the solution concentration (Figure 5.8 a). C_T as well as C_S exceed C_B at all concentrations between 10^{-6} and 1 x DPBS. Therefore, the influence of the platinum electrode potential is expected to dominate the SiNW conductance at all measured concentrations. The ratios C_B/C_S, C_B/C_T and $C_B/(C_T + C_S)$ were then plotted against the
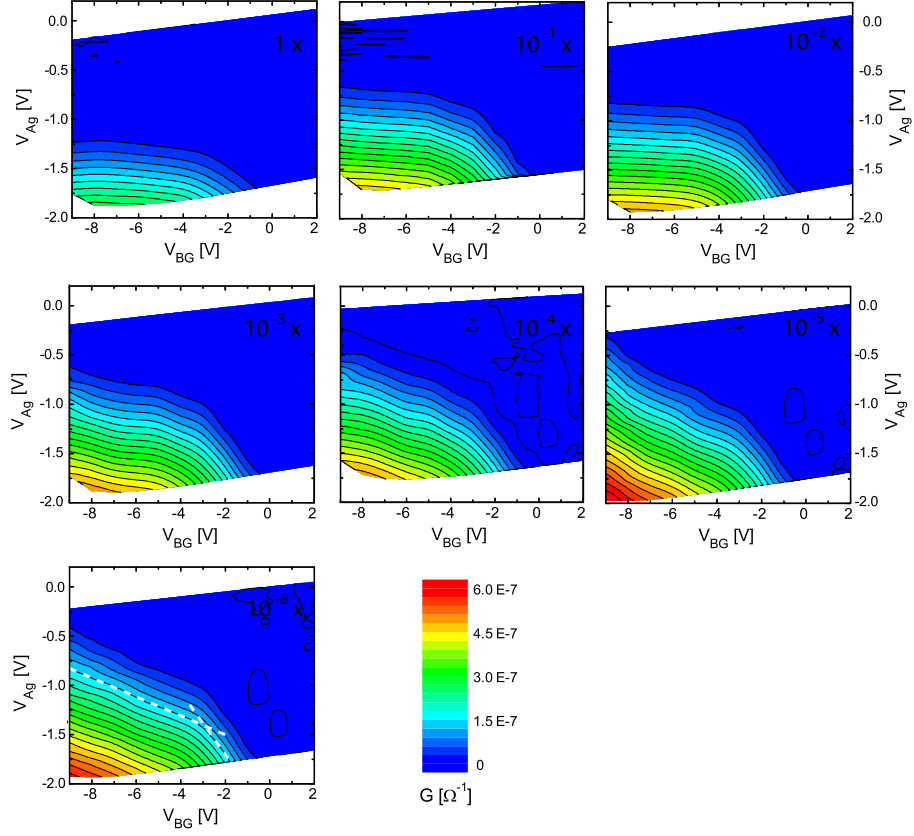
Figure 5.6: Contour plots of measurements with the 1 μm long SiNW in DPBS solutions. These measurements were conducted by directly sweeping the platinum electrode using the initial set-up. A silver wire acted as quasi-reference electrode. The top-left graph was obtained in undiluted DPBS, the following measurements were conducted in diluted DPBS with a dilution factor of 10 between each solution, down to a dilution of 10^{-6}. Two $\Delta V_{Ag}/\Delta V_{BG}$ ratios per DPBS concentration were determined at a conductance of $1.5 \cdot 10^{-7}$ Ω^{-1}. These two slopes are indicated by white dashed lines for 10^{-6} x DPBS. Contour level smoothing was enabled at all these plots.
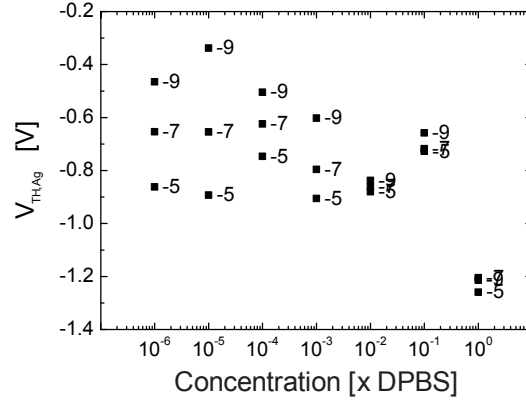
Figure 5.7: Threshold voltages relative to the silver wire potential at different DPBS concentrations.

Solution [x DPBS]	left slope ($\Delta V_{Ag}/\Delta V_{BG}$)	right slope ($\Delta V_{Ag}/\Delta V_{BG}$)	C_{DL} [F/m²]	λ_D [nm]
1	0.02	0.15	$9.5 \cdot 10^{-1}$	0.75
10^{-1}	0.02	0.27	$3.0 \cdot 10^{-1}$	2.4
10^{-2}	0.02	0.27	$9.5 \cdot 10^{-2}$	7.5
10^{-3}	0.05	0.30	$3.0 \cdot 10^{-2}$	24
10^{-4}	0.08	0.30	$9.5 \cdot 10^{-3}$	75
10^{-5}	0.12	0.30	$3.0 \cdot 10^{-3}$	240
10^{-6}	0.10	0.32	$9.5 \cdot 10^{-4}$	750

Table 5.2: $\Delta V_{Ag}/\Delta V_{BG}$ ratios, double layer capacitance and thickness (equals the Debye length) for different DPBS concentrations.

solution concentrations (Figure 5.8 b). Of course, these ratios do not accurately describe the situation, as the top oxide area is smaller than the side wall areas and the SiNW-BOX interface. Nevertheless, the measured $\Delta V_{Ag}/\Delta V_{BG}$ ratios left of the kink are close to the $C_B/(C_T + C_S)$ ratios. Between 10^{-5} and 10^{-6} x DPBS however, the capacitance ratios increase steeply while the measured ratio decreases. This could be caused by several influences that are not considered in this simplified model, such as the influence of the back-gate on the side and top walls of the SiNW, charges within the oxide layers and at the oxide-solution interfaces and the geometry of the nanowire and the parts of the leads that are exposed to the solution. Despite of the differences between the expected and the observed values at low concentrations, these measurements can qualitatively be explained by this simple model. This suggests that this SiNW is indeed capable of sensing the ion concentration of a solution.
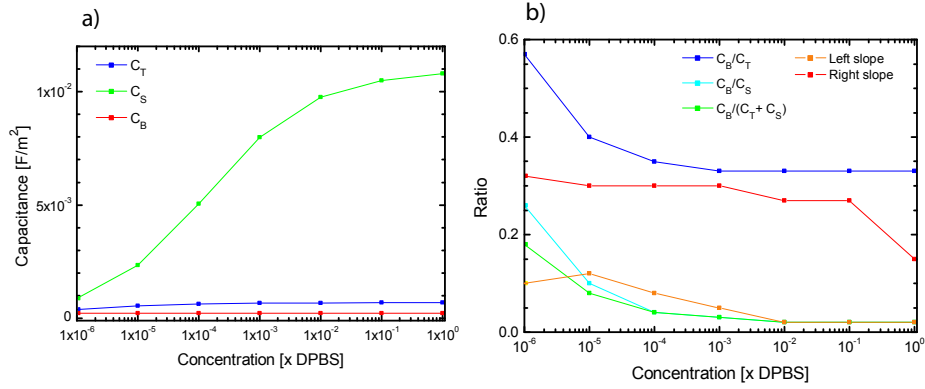
Figure 5.8: a) Capacitances of a SiNW in solutions for different DPBS concentration. These capacitance values for the top, side and bottom interfaces of the SiNW, C_T, C_S and C_B, respectively, were obtained using a simplified model described in Section 3.4. b) Ratios of these capacitances and comparison with the measured $\Delta V_{Ag}/\Delta V_{BG}$ ratios.

5.1.4   Stability of SiNWs and the calomel reference electrode

As shown above, the initial measurement set-up led to strongly shifting threshold voltages during solution measurements. The modified set-up, comprising a calomel reference electrode and a potentiostat, promises smaller reference potential fluctuations and therefore enhanced reproducibility of solution measurements.

In order to examine the improvements due to the modified set-up, the conductance stability of the 10 μm long nanowire was measured during four hours in pH 7 buffer, by sweeping $V_{Calomel}$ at $V_{BG} = -5$ V (Figure 5.9 a).

These measurements show the stability of the whole system, including the SiNW and the reference electrode. In order to reveal the stability of the reference electrode, the cyclovoltammogram of $Ru(NH_3)_6Cl_3$ was measured versus the calomel reference electrode before and after this SiNW measurement (Figure 5.9 b). Additional cyclovoltammograms were measured during a period of several weeks.

The SiNW stability measurements show a $V_{TH,Calomel}$ shift of about 75 mV during four hours, whit a maximal shift of 33 mV per hour.

The cyclovoltammograms on the other hand demonstrate the stability of the calomel electrode. The peaks and therefore also the measured $E^{0'}$ of the ruthenium compound of -210 mV versus the calomel electrode shifted about $\pm$ 5 mV within several weeks. Furthermore, there was no difference between the voltammograms that were measured before SiNW measurements and those measured afterward. This means that at least 65 mV of the $V_{TH,Calomel}$ shift have to originate from the SiNW itself.

It is known that ions are able to adsorb onto oxide-electrolyte interfaces, especially in accumulation, where negative gate voltages attract small cations such as K^+ [42, 43]. Such a charging of the oxide layers would cause a $V_{TH,Calomel}$ shift as it is observed.
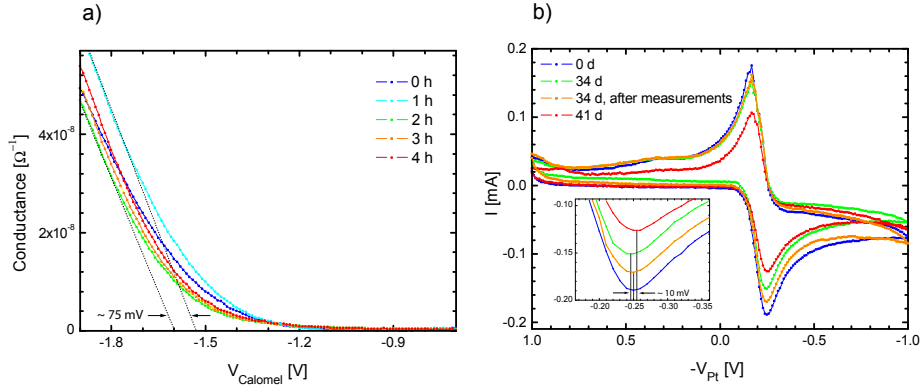
Figure 5.9: a) The stability of $V_{TH,Calomel}$ was examined by measuring the previously fabricated 10 μm long SiNW several times in pH 7 buffer solution during a time period of 4 hours. A shift of maximally 33 mV per hour was observed. b) Cyclovoltammogram of the ruthenium complex versus the calomel reference electrode. Such voltammograms were taken during several weeks, before and after measurements with SiNWs. During this period, the peeks shifted about $\pm$ 5 mV (inset).

5.2 Characterization of recently fabricated SiNWs

5.2.1 Nanowires characteristics on air

In the following section, the characteristics of recently fabricated SiNWs using the modified protocol (Section 2.1) will be presented and compared to the nanowires that had been fabricated previously. First, the transfer characteristics in air shall be discussed. A typical transfer characteristics sweep is shown in Figure 5.10. $V_{TH,p}$ and $V_{TH,n}$ were determined as -16.7 and 2.9 V from the linear plot (black). By using the slope of the same plot and an oxide capacitance of $1.2 \cdot 10^{-4}$ F/m^2, the device mobility was calculated to be 152 cm^2/Vs for holes in accumulation and 260 cm^2/Vs for electrons in the linear part of the inversion regime just above $V_{TH,n}$. While the mobility remained fairly constant at the accumulation side, it drastically dropped to about 20 cm^2/Vs in the inversion regime at back-gate voltage above 5 V. A subthreshold swing of 2.2 V per decade in depletion and 1.0 V per decade in weak inversion was obtained from the logarithmic plot (red). The accumulation conductance reached values of about $2 \cdot 10^{-7}$ Ω^{-1}, whereas the inversion conductance reached values of about $8 \cdot 10^{-8}$ Ω^{-1}. Furthermore, a small conductance peak within the depletion region was observed around -7 V.

These values significantly differ from those obtained from the previously fabricated 10 μm long nanowire. The most significant difference was observed at the accumulation regime, where $V_{TH,p}$ is around 12 V more negative and $\mu_{dev,h}$ about a third of the previously measured value. Moreover, S_D was about 17 times larger. The high $V_{TH,p}$ and subthreshold swing in depletion indicate a significant higher trap state density at the recently fabricated nanowire.
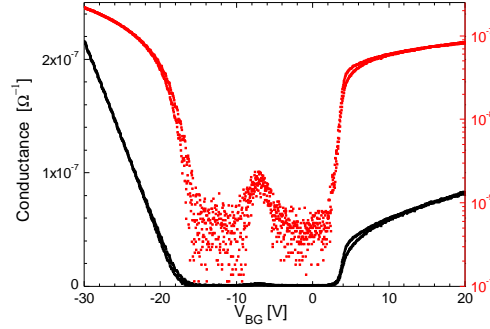
Figure 5.10: Logarithmic (red) and linear (black) plot of the transfer characteristics of a recently fabricated silicon nanowire with a width of 100 nm and length of 10 μm.

The inversion side on the other hand is similar to the one of the 1 μm long previously fabricated nanowire, although with a higher electron device mobility, which was however still much smaller than the mobility observed at the previously fabricated 10 μm long SiNW.

5.2.1.1 Geometry

The transfer characteristics in air of all functioning nanowires of a sample after bonding are shown in Figure 5.11. They were all 10 μm long, but had different widths from 100 nm to 1μm (Section 2.1.1). These measurements were done before applying epoxy.

The three thinner nanowires show similar behavior, whereas the widest SiNW shows no accumulation current at all, but very high depletion and inversion conductance. This behavior had not been observed before the nanowire was bonded. It is therefore most probably due to damages in the silicon device layer or the gate oxide caused by too much pressure applied on the contact pads while bonding.

When the three thinner SiNWs are compared, a $V_{TH,p}$ shift towards smaller voltages is observed with increasing width, especially between 100 and 125 nm width. Furthermore, the transconductance dG/dV_{BG} increased by a factor of 1.2 between these wires, whereas it is almost identical for the 125 and 150 nm wide wires.

The $V_{TH,p}$ shifts suggest that surface charges of the side walls have significant influence on the conductance of the nanowire: With decreasing width, this influence increases, hence $V_{TH,p}$ increases. This is in agreement with results obtained from previously fabricated SiNWs [20], as well as with the reported width-dependence of SOI-based SiNW conductance up to about widths of 150 nm [27] and the dependence of the conductance of SOI-based Si nanoribbons on their thickness [15] (in this case, the surface charges on the top of the ribbons influence V_{TH}).

In inversion, V_{TH} shifts much less, but it is the saturation conductance which increases with increasing width, except for the 125 nm and the 150 nm wide nanowires, which show about the same saturation conductance. The fact that this conductance is not constant for all widths, might again indicate that this saturation is caused by the nanowire itself instead of the leads or the contacts.
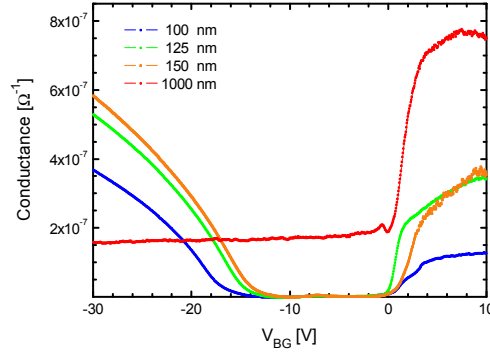
41

Figure 5.11: Transfer characteristics in air of a recently fabricated SiNW sample, measured after bonding, but before epoxy was applied. The widest nanowire was probably damaged during the bonding. $| V_{TH,p} |$ decreases and $\mu_{dev,h}$ increases with increasing width, whereas $V_{TH,n}$ remains relative constant.

However, even if most observations made during the above presented nanowire measurements somehow fit into the picture, the number of measured nanowires is probably too limited to draw any final conclusions.

5.2.1.2   SiNW Stability in air

After applying the epoxy, only the 100 nm wide SiNW survived. During the period of ten days, the transfer characteristics of this nanowire (now sealed with epoxy) were measured several times in air (Figure 5.12), usually before and after solution measurements. The inversion side of the graph turned out to be more stable, with a V_{TH} shift of maximally about 5 V. The saturation conductance was relatively stable throughout this measurement series. At the accumulation side, the device mobility varied significantly and V_{TH} shifted about 10 V.

This variations of V_{TH} and the device mobilities confirm the concerns about the interpretation of the measurements of SiNWs with different widths.

5.2.2   Characteristics in solution

All solution measurements with the recently fabricated 100 nm wide SiNW were performed using the modified set-up comprising a calomel reference electrode and the potentiostat. Contour plots of such a measurement in pH 7 buffer are shown in Figure 5.13. $V_{Calomel}$ was swept from -2 V to +1.5 V in steps of 10 mV at back-gate voltages between -30 and +22 V in steps of 4 V. In contrast to the previously fabricated SiNWs, a highly conductive accumulation region was not found in the measured potential window. The inversion region on the other hand already began at $V_{Calomel}$ around -1.7 V. As already observed at the accumulation region in contour plots of previously fabricated SiNWs, the inversion conductance suddenly decreased at $V_{BG} = 8$ V, which
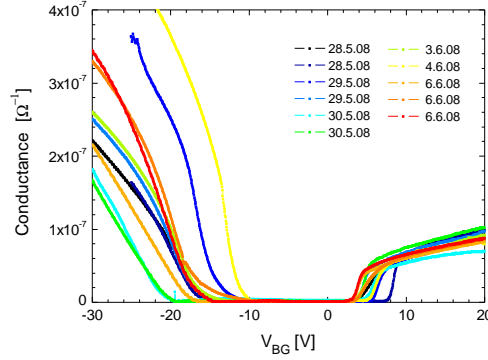
42

Figure 5.12: Transfer characteristics in air of a recently fabricated 100 nm wide SiNW, measured during a time period of 10 days. $V_{TH,p}$, $V_{TH,n}$ as well as the device mobilities strongly vary between different measurements.

leads to a kink of $\Delta V_{Calomel}/\Delta V_{BG}$ at constant conductance in Figure 5.13 a. As already discussed before, this is attributed to the parts of the sample that are not in contact with the solution. A $\Delta V_{Calomel}/\Delta V_{BG}$ ratio of 0.1 was manually extracted at $4 * 10^{-8}$ Ω^{-1} from the less steep slope on the right-hand side of the kink. The slope on the left-hand side of the kink was so steep, that the $\Delta V_{Calomel}/\Delta V_{BG}$ ratio could not be determined. This slope was also much steeper than the corresponding slope observed at previously fabricated SiNWs. It is in good agreement with the expected nearly infinitely steep slope due to a p-n junction within the leads (Figure 5.5).

As observed previously, the calomel reference potential nicely followed V_{Pt} at constant V_{BG}. The offset between these potentials remained relatively constant at a value of 300 mV at positive back-gate voltages and then linearly increased with decreasing V_{BG} up to 650 mV (Figure 5.13 b).

The current through the platinum electrode usually remained between around + 380 and - 130 nA (Figure 5.13 c).

The conductance in dependence of V_{BG} at constant $V_{Calomel}$ shows no saturation in inversion at negative $V_{Calomel}$ values (Figure 5.14 a). At positive calomel potentials, the slope of the inversion conductance only starts to become smaller close to the maximal applied back-gate voltage. The almost identical curves at $V_{Calomel}$ of +1 and +1.5 V show the small influence of the Pt electrode gate at this voltages.

When the conductance is plotted versus $V_{Calomel}$ (Figure 5.14 b), a saturation is visible at all V_{BG} values. The conductance near saturation become quite unstable.

These observations show that within the applied potential ranges, the conductance of the SiNW in solution is significantly influenced by the back-gate. The Pt electrode is only about 10 times as efficient as the back-gate which is five times less than observed in the accumulation region of previously fabricated SiNWs at a similar ion concentration (Section 5.1.3.1). Furthermore, the conductance becomes almost independent of $V_{Calomel}$ at $V_{Calomel} > 0$ for all back-gate voltages within the measured range.
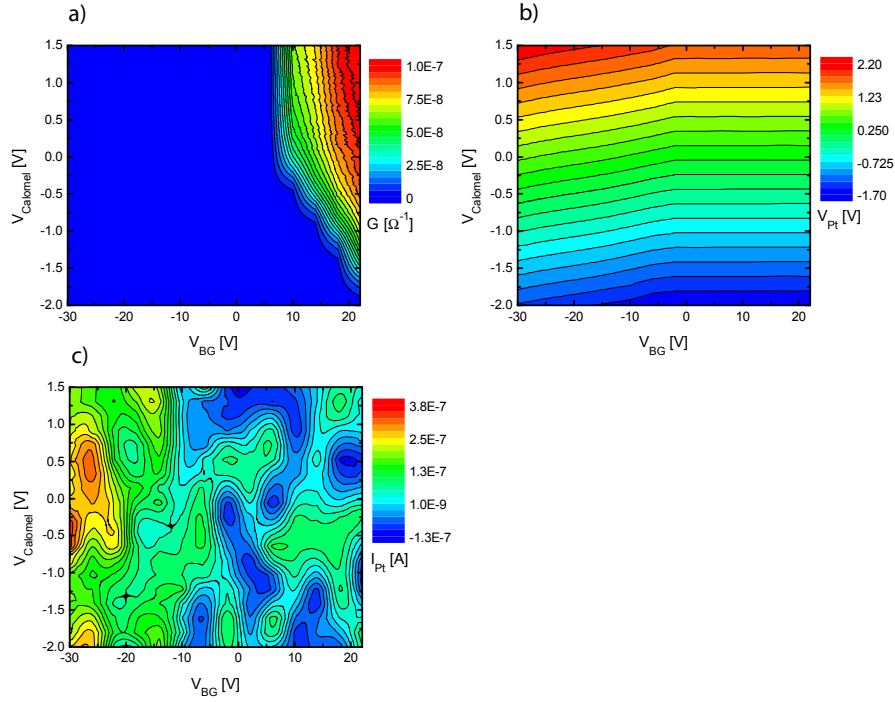
Figure 5.13: Contour plots of a measurement with a 100 nm wide recently fabricated SiNW in pH 7 buffer solution. a) The G vs. V_{BG} and $V_{Calomel}$ plot shows a region with high inversion conductance, but no accumulation region. b) V_{Pt} linearly follows $V_{Calomel}$ at constant V_{BG}, but with altering offset depending on V_{BG}. c) Current through the Pt electrode during the measurement. This data was plotted using contour level smoothing.
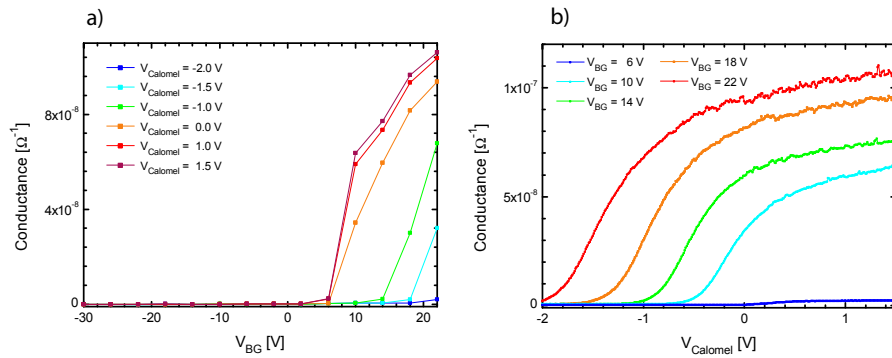

Figure 5.14: a) Conductance versus V_{BG} at different $V_{Calomel}$. The slope of the conductance starts to decrease at high V_{BG} values for positive $V_{Calomel}$. b) Conductance versus $V_{Calomel}$. The inversion conductance already increases at high negative $V_{Calomel}$ values. The conductance saturates at all measured V_{BG} values.

5.2.3 Concentration series & Capacitances

In order to test the sensing capabilities of this SiNW, the inversion region was measured in aqueous KCl solutions with concentrations of 10 μM, 1mM and 1 M. $V_{Calomel}$ was swept in steps of 10 mV from -1.5 V to 2 V at V_{BG} of 0, 2....20 V. Contour plots of these measurements are shown in Figure 5.15.

The $\Delta V_{Calomel}/\Delta V_{BG}$ ratio at $4 \cdot 10^{-8}$ Ω^{-1} was extracted manually from the contour plots. All three concentrations showed a ratio of 0.13 at the right-hand side of the kink. Not only the ratios were identical, but also the $V_{TH,Calomel}$ of these solutions at all V_{BG} were similar, with a shift of maximally about 50 mV (Figure 5.16).

A second series of measurements that was conducted some days later using the same solutions and SiNW, showed no $\Delta V_{Calomel}/\Delta V_{BG}$ dependence on the concentration as well and therefore confirmed the results of these measurements.

The ionic strength of the KCl concentrations used during these measurements correspond to those of $6 \cdot 10^{-5}$ x DPBS to 6 x DPBS. Comparing these results with those of the previously fabricated SiNWs, $\Delta V_{Calomel}/\Delta V_{BG}$ is expected to decrease at least between 10 μM KCl and 1 mM KCl. The ratio of about 0.13 observed at this measurement series is similar to the value obtained from the previously fabricated nanowires at 10^{-5} x DPBS.

The observed concentration independence within the measured concentration range could indicate a different ratio between the capacities C_T, C_S and C_B compared to the previously fabricated SiNWs. This could possibly lead to a concentration dependence only at higher or lower concentrations than the 10 μM to 1 M KCl range. This seems however improbable as the thickness of the top and buried oxide were measured to be quite homogeneous throughout the wafer (Section 2.1). The results could also indicate that the inversion conductance of this nanowire is dominated by any other effects such as trapped charges or contact resistance. In this case, the SiNW would not be suitable as a sensor.
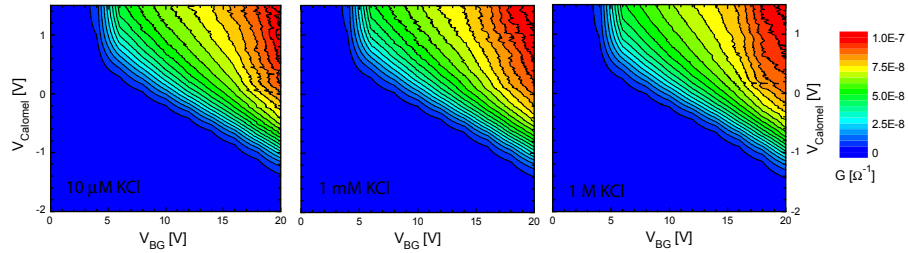

Figure 5.15: Contour plots of a recently fabricated 100 nm wide nanowire in aqueous solutions with KCl concentrations of 10 μM, 1 mM and 1M. The $\Delta V_{Calomel}/\Delta V_{BG}$ ratios do not depend on the ion concentration.
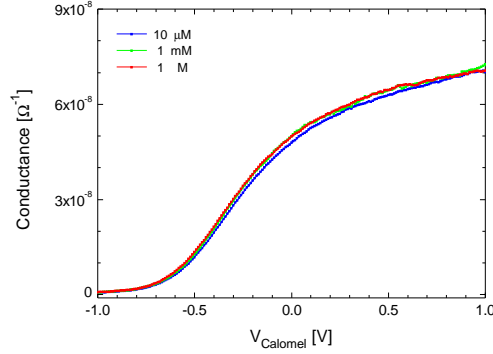
Figure 5.16: Conductance versus $V_{Calomel}$ at $V_{BG} = 14$ V for different KCl concentrations. The Conductance was very similar for all concentrations, with a maximal $V_{TH,Calomel}$ difference of about 50 mV.

5.2.4   pH measurements

After the concentration measurements could not prove the sensing capability of the recently fabricated SiNW, its response on a pH change of the measured solution was examined. Buffer solutions with pH 3 to 9 were measured in random order. Two of such measurement series were conducted at two different days, the first with pH 4, 7 and 9 buffer solutions, the second with pH 3,4..7 and 9 buffer solutions. $V_{Calomel}$ was swept in steps of 10 mV from -1.5 V to 2 V in at back-gate voltages of 0, 2...20 V. Contour plots of these measurements were almost identical to those already presented above and will therefore not be shown. $V_{TH,Calomel}$ was determined for each pH value at $V_{BG} = 8$, 14 and 20 V (Figure 5.17 a). These $V_{TH,Calomel}$ values of all pH buffer solutions relative to $V_{TH,Calomel}$ at pH 4 are shown in Figure 5.17 b. Theoretically, a $V_{TH,Calomel}$ shift towards more positive voltages is expected with increasing pH value. This is due the increasing number of negatively charged $SiOH^-$ groups on the oxide surface with increasing pH (Section 3.3). Therefore a more positive liquid potential has to be applied in order to drive the SiNW into inversion. The shift observed during both measurement series is mostly in agreement with theory. However, during the second measurement series in pH 3..9 buffer solutions, $V_{TH,Calomel}$ did not significantly shift between pH 5 and 7. The average $V_{TH,Calomel}$ shift was 30 and 25 mV/pH at the first and second measurement series, respectively. This is about half of the maximal reachable value of 59 mV/pH. This average shift is however in good agreement with the usually observed shift of around 30 mV per pH unit for SiO_2 [2]. Individual shifts exactly reached 59 mV/pH (pH 7 to 9). Shifts larger than this maximally expected value were not observed.

In order to test the significance of these results, the pH 5 buffer solution was measured four times during the second measurement series. G vs. $V_{Calomel}$ plots at $V_{BG} = 14$ V of these measurements are shown in Figure 5.18 a. The right image shows the $V_{TH,Calomel}$ shift relative to the first measurement. These shift reached values of up to 90 mV, which is more than halve of the $V_{TH,Calomel}$ shift measured between pH 3 and pH 9. This was however only one measurement, the three other measurements showed a shift of less than 40 mV.
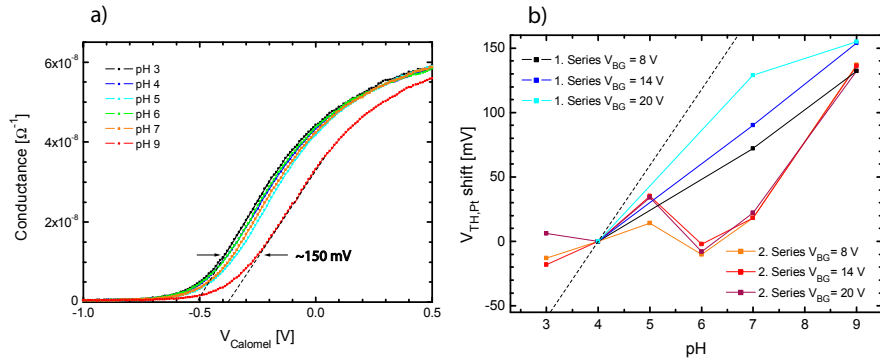
46

Figure 5.17: Recently fabricated 100 nm wide SiNW measured in pH buffer solutions. a) Conductance versus $V_{Calomel}$ at $V_{BG} = 14$ V. The $V_{TH,Calomel}$ shift is indicated by dashed black lines. b) $V_{TH,Calomel}$ values of both pH measurement series at $V_{BG} = 8$, 14 and 20 V, relative to $V_{TH,Calomel}$ at pH 4. The dashed black line indicates the maximal reachable value of 59 mV/pH.
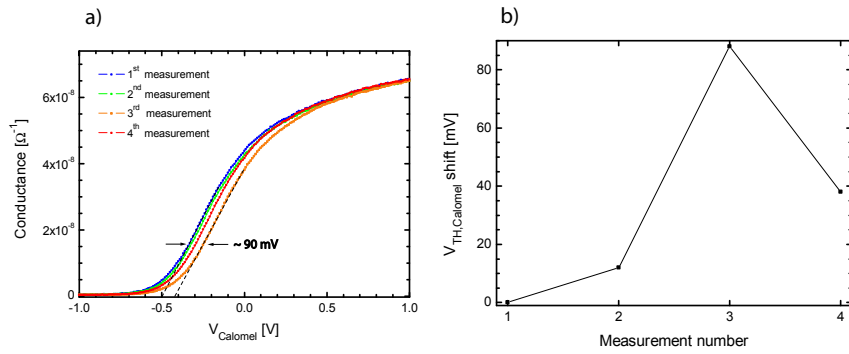
Figure 5.18: Measurements in pH 5 buffer in order to determine the stability of a recently fabricated 100 nm wide SiNW. a) G versus $V_{Calomel}$ at $V_{BG} = 14$ V. The $V_{TH,Calomel}$ shift is indicated by dashed black lines. b) $V_{TH,Calomel}$ shifts during these four measurements.

Concluding, it could be said, that this recently fabricated SiNW, measured using the modified set-up with potentiostat and Calomel reference electrode, indeed is capable of sensing pH changes. Issues such as relatively high shifts between measurements at the same pH however still remain.

47

Chapter 6

Conclusions & Outlook

Using previously fabricated SiNWs, a influence of the ion concentration of the measured solution on the SiNW conductance was observed. The coupling efficiency of the electrolyte-gate relative to the back-gate increased from a factor of ten at 10^{-6} x DPBS to fifty at 1 x DPBS. These results were in good agreement with values obtained from a simple model considering capacitance ratios during SiNW measurements in solution.

After initial issues, new SiNWs were successfully fabricated. Their characteristics however deviated from the previously fabricated SiNWs. Particularly, no highly conductive accumulation region was observed during measurements in solution. As the number of functioning SiNWs was very limited and only a single SiNW could be examined in solution, it is however not clear, whether the difference in characteristics stems from the modified fabrication protocol or if it is due to sample-to-sample variation.

The pH sensitivity of these recently fabricated SiNWs could be demonstrated with a voltage shift of 25 to 30 mV/pH, which is in line with reported values for SiO_2-coated ISFETs [2]. These measurements were only possible due to the improved stability of the measurement set-up by implementing a calomel reference electrode and a potentiostat to control the electrode potentials. This significantly reduced threshold voltages shifts in solution compared to measurements conducted with the initial set-up comprising an Ag wire quasi-reference electrode. However, threshold voltage shifts were still in the order of tens of mV during measurements at constant pH and ion concentration. This is probably due to trap states within the oxide that originate from the fabrication process or due to ion adsorption onto the oxide-electrolyte interface. SiNW measurements in air before and after measurements in solution also showed strongly varying V_{TH} values and therefore supported this assumption.

An important step to increase the stability and reliability of SiNW sensors will therefore be to remove the top oxide and the native oxide at the SiNW side walls and to oxidize these surfaces in a controlled manner in order to obtain homogeneous, well-defined semiconductor-oxide interfaces. Furthermore, by using lithography, the leads could completely be covered with a dielectric. That way, only the SiNWs would be exposed to the solution, which would facilitate the interpretation of measurement results and decrease the sample-to-sample variation due to the manually applied epoxy.

The statistical analysis of measurements of several SiNWs in parallel would be another method to further increase the significance of measurement result. Such sensor arrays decrease the influence of fluctuations of single sensors and therefore enhance the sensitivity and reliability [10, 44]. By adding multiplexers to the measurement set-up, a first step towards SiNW array measurements has been done during this project.

Besides these suggested modifications for the near future, there is still a long way to go in order to reach stable and reliable fully integrated SiNW sensors. The most noteworthy challenges ahead will be the integration of the reference and platinum electrodes on the chip [45], as well as control of the local temperature and fluid flow.

Danksagung

An dieser Stelle möchte ich mich bei allen, die zum Gelingen dieser Arbeit beigetragen haben, herzlich bedanken: Zu allererst bei Christian Schönenberger für die Möglichkeit, meine Masterarbeit in seiner Forschungsgruppe durchführen zu dürfen. Ich bedanke mich besonders auch bei Michel Calame, Dino Keller und Oren Knopfmacher, die mich während meiner Arbeit mit viel Geduld betreut haben. Bei Dominik Zumbühl möchte ich mich dafür bedanken, dass er sich als Beisitzer für meine Masterprüfung zur Verfügung gestellt hat. Michael Steinacher und Heinz Breitenstein, sowie ihren Mitarbeitern bei den verschiedenen Werkstätten der Universität Basel gebührt Dank dafür, dass sie mir jederzeit mit Rat und Tat weitergeholfen haben und besonders auch für das Anfertigen einer neuen Flüssigzelle und des massgeschneiderten Potentiostaten. Dank gebührt natürlich auch allen Mitgliedern der Forschungsgruppen von Christian Schönenberger und Dominik Zumbühl, die nicht nur für eine sehr angenehme Stimmung in den Büros und den Labors sorgten, sondern mir auch bei allfälligen Fragen und Problemen stets hilfreich weiterhalfen.

Appendix A

Fabrication issues and protocol details

A.1 Issues of the initial protocol

The initial fabrication protocol used a combination of UV and e-beam lithography to pattern the SiNWs and their leads [20]. A chromium film was deposited by evaporation after each of these subsequent lithography steps. This led to a height step within the metal film at the intersections of those two patterns. For unknown reasons, the chromium layer showed a small crack at exactly this step. This crack was then transferred to the silicon dioxide top layer and finally the silicon device layer by plasma and TMAH etching, respectively (Figure A.1). This usually led to a complete disconnection of all nanowires of one sample. Interestingly, these cracks only occurred at one lead per nanowire and always at the same side within a sample.

This leads to the conclusion that an anisotropy either during evaporation or the UV lithography probably caused this effect. This problem was avoided by patterning the SiNWs as well as the leads by e-beam lithography. As a positive side effect, this change also eliminated one evaporation step and the time consuming alignment of UV and e-beam lithography masks.

Another critical fabrication step was the wet etching of the silicon device layer. As the TMAH etch rate of silicon is very sensitive to several factors such as flow rate, temperature and concentration [33], it is important to accurately control these parameters. Initially the samples were just thrown into the liquid without any control about their orientation. Usually they were sticking to the glass walls of the beaker and were eventually dragged into the stirrer by the liquid flow. This often led to severe scratches on the samples, which usually rendered them unusable. To prevent this problem, teflon tweezers that held the samples at a fixed place were constructed by the mechanics workshop. Furthermore, these tweezers led to a higher stability of the etch rate.
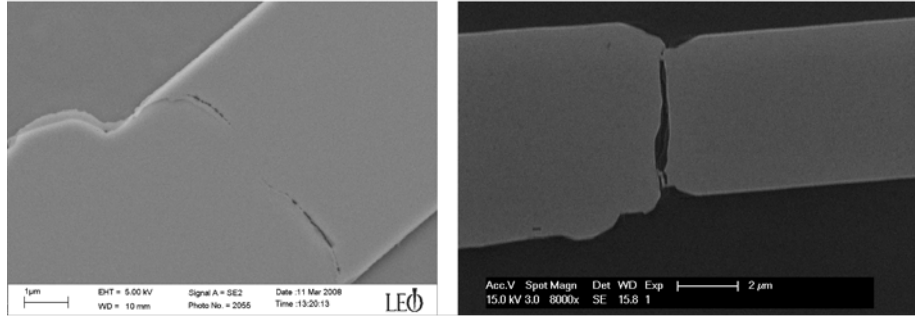
Figure A.1: SEM images of cracks in the top oxide and Si device layer of SiNW leads. These cracks occurred at the intersection of UV and e-beam lithography.

A.2   The modified protocol

1. Chrome mask

   (a) Clean sample: 5 min sonication in acetone and isopropanol, UV/ozone for 10 min and 5 min sonication in acetone and isopropanol again.

   (b) Spin coat 950k-PMMA from chlorobenzene at 4000 rpm for 40 s. Adjust PMMA concentration, such that the layer has a thickness of 320 nm. Bake for 30 min at 170° C.

   (c) E-beam lithography (JEOL JSM-IC 848 with Raith ELPHY Quantum software) at 35 kV acceleration voltage and following exposure parameters:

Parameter	Large mask	Small mask
Area dose [$\mu As/cm^2$]	400	400
Line dose [$\mu As/cm$]	-	2400
Ares step size [nm]	256	10
Line step size [nm]	-	2
Probe current [A]	10^{-6}	10^{-10}

   Table A.1: e-beam exposure parameters

   (d) Develop for 90 s in MIBK:isopropanol 1:3, wash in isopropanol.

   (e) Chromium evaporation (Balzers-Pfeiffer PLS 500): 60 nm, at about $5 \cdot 10^{-7}$ mbar and 0° C. Deposition rate about 0.2 nm/s.

   (f) Lift-off for 1h in acetone at 45° C.

2. SiO$_2$ plasma etch (Plasmalab 80 Plus): All steps at 25 mTorr and a base pressure of $5 \cdot 10^{-5}$ mbar.

   (a) 2 min, 16 % O$_2$, 100 W

   (b) 1 min 30 s, 40 % CHF$_3$ + 2 % O$_2$, 100 W

   (c) 2 min, 40 % CHF$_3$, 100 W

   (d) 2 min, 16 % O$_2$, 100 W

3. Remove Cr

   (a) 10 min in a solution of 2.40 g NaOH and 3.16 g KMnO$_4$ in 21 ml H$_2$O, shaking

   (b) 2 min in H$_2$O, shaking

   (c) Wash three times in H$_2$O and then in isopropanol

4. Device layer etching

   (a) Remove native oxide
      i. Dip 1 min in H$_2$O to wet surface
      ii. 20 s in a solution of 21 ml HF (40% in H$_2$O), 148 ml H$_2$O and 155 g NH$_4$F
      iii. Wash three times in H$_2$O, then in isopropanol

   (b) Si etch
      i. 12 min in a solution of 90 % TMAH (25% in H$_2$O) and 10 % isopropanol at 45° C while vigorous stirring with 200 rpm.
      ii. Wash three times in H$_2$O (only short dip in the first bath), then in isopropanol

5. Contacts

   (a) Spin-coat hexamethyldisilazane (HMDS), then negative-photoresist (ma-N 415 from Micro Resist Technology), each at 4000 rpm and for 40 s, bake for 90 s at 100° C.

   (b) UV lithography: expose sample for 60 s.

   (c) Develop for 70 s (ma-D 332S from Micro Resist Technology), wash in H$_2$O.

   (d) UV/ozone for 5 min.

   (e) 5 min in a solution of 21 ml HF (40% in H$_2$O), 148 ml H$_2$O and 155 g NH$_4$F.

   (f) Wash three times in H$_2$O.

   (g) 30 s of Ar plasma in the evaporator at around $5 \cdot 10^{-7}$ mbar.

   (h) Deposit 100 nm of aluminum by evaporation at about -20° C and $1 \cdot 10^{-7}$ mbar at a deposition rate of around 1 nm/s.

   (i) Anneal sample in forming gas (using a MBE Komponenten GmbH AZ 500 annealing oven) with the following recipe:
      i. 60 s at 120° C, Process type 4
      ii. 60 s at 120° C, Process type 3
      iii. 600 s at 120° C, Process type 1
      iv. 600 s at 450° C, Process type 1

6. Packaging

   (a) Connect back-gate (i.e. the Si substrate) by scratching the sample and applying silver paint.

   (b) Bond SiNWs and the back-gate to pins of a chip carrier.

   (c) Manually seal all metallic contact pads and bonds with epoxy (EPO-TEK 303-2M), let epoxy dry over night at room temperature.

Appendix B

The SP 920 Potentiostat

The SP 920 potentiostat was designed and fabricated by the electronics workshop of the University of Basel. All connections to the potentiostat as well as all indicators and switches are positioned on its front panel (Figure B.1). The diagram on this panel describes the mode of operation of the potentiostat: By a feedback loop, the voltage that is applied at the counter electrode V_{out} (also denoted as "Voltage Out to Electrode") is altered until "Set Voltage In" equals "Ref. Electrode Voltage In" (the difference between these two voltages can be monitored by using the "Error Volt. Out" output). The feedback loop can manually be adjusted to a bandwidth between 0.1 Hz and 1 kHz. It can be switched on and off manually or by an external TTL signal. The output current can be limited to either 1 μA, 10 μA or 10 mA. The output voltage is limited to ± 2 V. Using the two outputs "Current Control Out" and "Voltage Control Out", the output current and voltage can be monitored. A detailed schematic of the potentiostat is shown in Figure B.2.

Figure B.1: Front panel of the potentiostat

54

Figure B.2: Schematic of the SP 920 potentiostat

Bibliography

[1] P. Bergveld, "Development of an ion-sensitive solid-state device for neurophysiological measurements," *IEEE Trans. Biomed. Eng.*, vol. 17, p. 70, 1970.

[2] P. Bergveld, "Isfet, theory and practice," in *IEEE Sensor Conference Toronto*, 2003.

[3] W. Sant, M. Pourciel-Gouzy, J. Launay, T. D. Conto, R. Colin, A. Martinez, and P. Temple-Boyer, "Development of a creatinine-sensitive sensor for medical analysis," *Sens. Actuators B*, vol. 103, p. 260, 2004.

[4] A. Kharitonov, M. Zayats, A. Lichtenstein, E. Katz, and I. Willner, "Enzyme monolayer-functionalized field effect transistor for biosensor applications," *Sens. Actuators B*, vol. 70, p. 222, 2000.

[5] E. Souteyrand, J. P. Cloarec, J. R. Martin, C. Wilson, I. Lawrence, S. Mikkelson, and M. F. Lawrence, "Direct detection of the hybridization of synthetic homo-oligomer dna sequences by field effect," *J. Phys. Chem. B*, vol. 101, p. 2980, 1997.

[6] M. W. Shinwari, M. J. Deen, and D. Landheer, "Study of the electrolyte-insulator-semiconductor field-effect transistor (eisfet) with applications in biosensor design," *Microelectronics Reliability*, vol. 47, pp. 2025–257, 2007.

[7] C. M. Niemeyer and D. Blohm, "Dna microarrays," *Angew. Chem. Int. Ed.*, vol. 38, p. 2865, 1999.

[8] A. K. Wanekaya, W. Chen, N. V. Myung, and A. Mulchandani, "Nanowire-based electrochemical biosensors," *Electroanalysis*, vol. 18, p. 533, 2006.

[9] F. Patolsky, B. Timko, G. Yu, Y. Fang, A. Greytank, G. Zheng, and C. Lieber, "Detection, stimulation, and inhibition of neuronal signals with high-density nanowire transistor arrays," *Science*, vol. 313, p. 1100, 2006.

[10] M. C. McAlpine, H. Ahmad, D. Wang, and J. R. Heath, "Highly ordered nanowire arrays on plastic substrates for ultrasensitive flexible chemical sensors," *Nature Materials*, vol. 6, p. 379, 2007.

[11] A. A. Talin, L. L. Hunter, F. Leonard, and B. Rokad, "Large area, dense silicon nanowire array chemical sensors," *Appl. Phys. Lett.*, vol. 89, p. 153102, 2006.

[12] F. Patolsky, G. Zheng, O. Hayden, M. Lakadamyali, X. Zhuang, and C. M. Lieber, "Electrical detection of single viruses," *PNAS*, vol. 101, p. 14017, 2004.

[13] Z. Li, Y. Chen, X. Li, T. I. Kamins, K. Nauka, and R. S. Williams, "Sequence-specific label-free dna sensors based on silicon nanowires," *Nano Lett.*, vol. 4, p. 245, 2004.

[14] E. T. Carlen and A. van den Berg, "Nanowire electrochemical sensors: can we live without labels?," *Lab Chip*, vol. 7, p. 19, 2007.

[15] N. Elfstroem, A. E. Karlstrom, and J. Linnros, "Silicon nanoribbons for electrical detection of biomolecules," *Nano lett.*, vol. 8, p. 945, 2008.

[16] I. Heller, A. M. Janssens, J. Mannik, E. D. Minot, S. G. Lemay, and C. Dekker, "Identifying the mechanism of biosensing with carbon nanotube transistors," *Nano Lett.*, vol. 8, p. 591, 2008.

[17] A. Star, J. Gabriel, K. Bradley, and G. Gruner, "Electronic detection of specific protein binding using nanotube fet devices," *Nano Lett.*, vol. 3, p. 459, 2003.

[18] H. Im, X.-J. Huang, B. Gu, and Y.-K. Choi, "A dielectric-modulated field-effect transistor for biosensing," *Nature Nanotechnology*, vol. 2, p. 430, 2007.

[19] X. Liang and S. Y. Chou, "Nanogap detector inside nanofluidic channel for fast real-time label-free dna analysis," *Nano Lett.*, vol. 8, p. 1472, 2008.

[20] D. Keller, *Nano Field Effect Transistors as basic building blocks for sensing*. PhD thesis, University of Basel, 2007.

[21] E. Stern, J. F. Klemic, D. A. Routenberg, P. N. Wyrembak, D. B. Turner-Evans, A. D. Hamilton, D. A. LaVan, T. M. Fahmy, and M. A. Reed, "Label-free immunodetection with cmos-compatible semiconducting nanowires," *Nature*, vol. 445, p. 519, 2007.

[22] O. H. Elibol, D. Morisette, D. Akin, J. P. Denton, and R. Bashir, "Integrated nanoscale silicon sensors using top-down fabrication," *Appl. Phys. Lett.*, vol. 83, p. 4613, 2003.

[23] G. K. Celler and S. Cristoloveanu, "Frontiers of silicon-on-insulator," *J. Appl. Phys.*, vol. 93, p. 4955, 2003.

[24] E. Stern, R. Wagner, F. Sigworth, R. Breaker, T. M. Fahmy, and M. A. Reed, "Importance of the debye screening length on nanowire field effect transistor sensors," *Nano lett.*, vol. 7, p. 3405, 2007.

[25] P. R. Nair and M. A. Alam, "Screening-limited response of nano-biosensors," *Nano Lett.*, vol. 8, p. 1281, 2008.

[26] Y. Chen, X. Wang, S. Erramilli, P. Mohantya, and A. Kalinowski, "Silicon-based nanoelectronic field-effect ph sensor with local gate control," *Appl. Phys. Lett.*, vol. 89, p. 223512, 2006.

[27] N. Elfstrom, R. Juhasz, I. Sychugov, T. Engfeldt, A. E. Karlstrom, and J. Linnros, "Surface charge sensitivity of silicon nanowires: Size dependence," *Nano lett.*, vol. 7, p. 2608, 2007.

[28] M. Lemme, T. Mollenhauer, W. Henschel, T. Wahlbrink, M. Heuser, M. Baus, O. Winkler, B. Spangenberg, R. Granzner, F. Schwierz, and H. Kurz, "Influence of channel width on n- and p-type nano-wire-mosfets on silicon on insulator substrate," *Microelectron. Eng.*, vol. 67-68, p. 810, 2003.

[29] P. R. Nair and M. A. Alam, "Design considerations of silicon nanowire biosensors," *IEEE Transactions On Electron Devices*, vol. 54, p. 3400, 2007.

[30] O. Knopfmacher, "Development of soi-wafer based nanowire field effect transistors for sensor applications," Master's thesis, University of Basel, 2007.

[31] W. Sonphao and S. Chaisirikul, "Silicon anisotropic etching of tmah solution," *Industrial Electronics, 2001. Proceedings. ISIE 2001. IEEE International Symposium on*, vol. Volume 3, pp. 2049 – 2052, 2001.

[32] I. Zubel and M. Kramkowska, "The effect of isopropyl alcohol on etching rate and roughness of (100) si surface etched in koh and tmah solutions," *Sensors and Actuators A*, vol. 93, pp. 138–147, 2001.

[33] O. Tabata, R. Asahi, H. Fuabashi, K. Shimaoka, and S. Sugiyama, "Anisotropic etching of silicon in tmah solutions," *Sensors and Actuators A*, vol. 34, pp. 51–57, 1992.

[34] S. M. Sze and N. K. Kwok, *Physics of Semiconductor Devices*. John Wiley & Sons, Inc., 2007.

[35] J. P. Colinge and C. A. Colinge, *Physics of Semiconductor Devices*. Cluwer Academic Publisher, 2002.

[36] C. E. Housecroft and A. G. Sharpe, *Inorganic Chemistry*. Prentice Hall, 2007.

[37] A. Bard and L. Faulkner, *Electrochemical Methods - Fundamentals and Applications*. John Wiley & Sons, Inc., 2001.

[38] O.Wunnicke, "Gate capacitance of back-gated nanowire field-effect transistors," *Appl. Phys. Lett.*, vol. 89, p. 083102, 2006.

[39] D. Landheer, G. Aers, W. R. McKinnon, M. J. Deen, and J. C. Ranuarez, "Model for the field effect from layers of biological macromolecules on the gates of metal-oxide-semiconductor transistors," *J. Appl. Phys*, vol. 98, p. 44701, 2005.

[40] P. Bergveld, "Thirty years of isfetology. what happened in the past 30 years and what may happen in the next 30 years," *Sensors and Actuators B*, vol. 88, p. 1, 2003.

[41] S. Cristoloveanu, "A review of the pseudo-mos transistor in soi wafers: Operation, parameter extraction, and applications," *IEEE Transactions On Electron Devices*, vol. 47, p. 1018, 2000.

[42] D. A. Sverjensky, "Prediction of surface charge on oxides in salt solutions: Revisions for 1:1 (m l) electrolytes," *Geochimica et Cosmochimica Acta*, vol. 69, p. 225, 2005.

[43] M. Rentschler and P. Fromherz, "Membrane-transistor cable," *Langmuir*, vol. 14, p. 547, 1998.

[44] C. Gentil, G. Philippin, and U. Bockelmann, "Signal enhancement in electronic detection of dna hybridization," *Phys. Rev. E*, vol. 75, p. 011926, 2007.

[45] A. Simonis, *Untersuchungen zur Entwicklung einer feldeffektbasierten Biosensoranordnung mit integriertem Referenzsystem.* PhD thesis, Rheinisch-Westfaelische Technische Hochschule Aachen, 2006.